

5.1.2 Breakthrough with Radioactive Decay

For all 12 radionuclides representing the first five cases, the results for flow and transport are tabulated in Table 5.3. The normalized peaks of expected mass flux and concentration ($\langle Q \rangle_{\max}$, $\langle q \rangle_{\max}$, and $\langle C \rangle_{\max}$) at the seafloor, and the peaks of the standard deviations ($(\sigma_Q)_{\max}$, $(\sigma_q)_{\max}$, and $(\sigma_C)_{\max}$) are listed in the table. Also the times and locations at which these peaks occur are presented. Table 5.3a displays the statistics related to $Q(t)$ and $q(x, t)$, whereas Table 5.3b shows the statistics of the concentration $C(x, t)$. In addition, the uncertainties associated with arrival times and locations are given in the last two columns of Table 5.3b. The flux and concentration values include radioactive decay and are based on unit mass at the source. Radionuclides in Case 1 have no retardation and 100 percent hydraulic release, which means that all particles are released to the flow field and allowed to move at the same time. Figure 5.15 gives the flux and concentration results for tritium, ^3H , which is an element in Case 1. The short travel times (without matrix diffusion effect) to the seafloor result in essentially little decay (if any) even with the short half-life of ^3H . However, adding the matrix diffusion effect yields a delayed arrival and allows for more radioactive decay. Figure 5.15 shows that the mean concentration distribution has a peak value of about 1.6×10^{-8} times the initial source concentration, C_0 . Adding one standard deviation to this value leads to a normalized peak of about 3.0×10^{-7} . This peak occurs roughly 110 years after the test and at about 4,500 m from the island center (about 2,440 m from the shoreline).

As alluded to earlier, matrix diffusion leads to delayed arrival of mass and lower mass fluxes. This delayed arrival encounters significant decay for short-lived nuclides. The effect of this parameter is much less dramatic for radionuclides with long half-lives. Carbon-14, with a half-life about three orders of magnitude longer than tritium, shows significant mass flux and peak concentration as compared to ^3H with $\kappa = 0.434$. The normalized peak of the mean concentration is found to be about 1.4×10^{-4} , as shown in Figure 5.16, and occurs at about 700 years and the same location as for ^3H .

Classes 2 to 5 include a portion of slow release due to glass dissolution with different ratios of hydraulic/geochemical release. To show the effect of the slow release ratio, the results for an element in Class 1 (with 100 percent hydraulic release) are compared to those of an element in Class 3 with 60 percent hydraulic release and 40 percent slow release via glass dissolution. Figure 5.17 compares the total mass flux decayed breakthrough curves ($\langle Q(t) \rangle$) for ^{85}Rb from Class 1 and ^{90}Zr from Class 3. These two elements are selected because they both are stable daughters and thus the effect of different half-lives can be removed. The top plot of Figure 5.16 is for $\kappa = 0.434$ and the lower plot is for $\kappa = 0.0434$. As is clear from the figure, the different values of mass flux are the result of releasing all the mass instantaneously in the case of ^{85}Rb but releasing only 60 percent of the mass and holding 40 percent in glass puddle in the case of ^{90}Zr . The figure also exhibits the effect of changing the matrix diffusion parameter κ by an order of magnitude. That change results in a two-orders-of-magnitude change in the resulting mass flux for both elements presented in the figure. Again, a thorough sensitivity analysis for the effect of κ is presented in Section 6.1.2.

Table 5.3a. Peaks of expected and standard deviation of mass flux and the associated times and locations for radionuclides in the Milrow source term. The elements in Class 6 are completely decayed.

Case	Radio-nuclide	Half-life	$\langle Q \rangle_{\max}$	Time	$(\sigma_Q)_{\max}$	Time	$\langle q \rangle_{\max}$	Time	Location	$(\sigma_q)_{\max}$	Time	Location
1	^3H	4.49e+03	5.9160e-014	9.2055e+001	1.0179e-012	9.2055e+001	1.8000e-016	8.4932e+001	4.3800e+003	3.1125e-015	8.4932e+001	4.3800e+003
	^{14}C	2.09e+06	4.9531e-010	6.9151e+002	8.0008e-009	6.3397e+002	1.2846e-012	6.5973e+002	4.6600e+003	2.2213e-011	6.5973e+002	4.6600e+003
	^{85}Kr	3.91e+03	2.8176e-014	8.6027e+001	4.8505e-013	8.5479e+001	9.0552e-017	7.9452e+001	4.3800e+003	1.5658e-015	7.9452e+001	4.3800e+003
	^{85}Rb	stable	5.4081e-010	7.6548e+002	8.6625e-009	6.8055e+002	1.3952e-012	7.0630e+002	4.6600e+003	2.4125e-011	7.0630e+002	4.6600e+003
2	^{36}Cl	1.10e+08	2.6456e-010	7.7753e+002	4.2340e-009	6.9041e+002	6.1266e-013	6.6301e+002	4.6200e+003	1.0594e-011	6.6247e+002	4.6200e+003
	^{129}I	5.73e+09	2.6502e-010	7.7973e+002	4.2406e-009	6.9151e+002	6.1358e-013	6.6356e+002	4.6200e+003	1.0610e-011	6.6356e+002	4.6200e+003
3	^{90}Sr	1.06e+04	1.1926e-012	1.4192e+002	2.0386e-011	1.4192e+002	3.0254e-015	1.3753e+002	4.4600e+003	5.2315e-014	1.3753e+002	4.4600e+003
	^{90}Y	2.67e+00	3.0048e-016	1.4192e+002	5.1362e-015	1.4192e+002	7.6226e-019	1.3753e+002	4.4600e+003	1.3181e-017	1.3753e+002	4.4600e+003
	^{90}Zr	stable	3.2052e-010	7.7425e+002	5.1450e-009	6.9205e+002	7.3707e-013	6.8548e+002	4.6200e+003	1.2745e-011	6.8548e+002	4.6200e+003
4	^{99}Tc	7.78e+07	1.0539e-010	7.8575e+002	1.6861e-009	6.9315e+002	2.8500e-013	6.6740e+002	4.6200e+003	4.9281e-012	6.6740e+002	4.6200e+003
5	^{137}Cs	1.10e+04	1.9012e-012	1.4247e+002	3.2552e-011	1.4192e+002	5.5168e-015	1.3205e+002	4.4600e+003	9.5394e-014	1.3205e+002	4.4600e+003
	^{137}Ba	stable	4.3375e-010	7.8082e+002	6.9370e-009	6.9479e+002	1.0198e-012	6.8055e+002	4.5800e+003	1.7635e-011	6.8055e+002	4.5800e+003

Table 5.3b. Peaks of expected and standard deviation of concentration and the associated times and locations for radionuclides in the Milrow source term. The elements in Class 6 are completely decayed.

Case	Radio-nuclide	Half-life	$\langle C \rangle_{\max}$	Time	Location	$(\sigma_C)_{\max}$	Time	Location	σ_{Time}	σ_{Location}
1	^3H	4.49e+03	1.6935e-008	8.4932e+001	4.3800e+003	2.9283e-007	8.4932e+001	4.3800e+003	1.9774e+002	4.6744e+002
	^{14}C	2.09e+06	1.4840e-004	6.5973e+002	4.6600e+003	2.5661e-003	6.5973e+002	4.6600e+003	1.9774e+002	4.6744e+002
	^{85}Kr	3.91e+03	8.5191e-009	7.9452e+001	4.3800e+003	1.4731e-007	7.9452e+001	4.3800e+003	1.9774e+002	4.6744e+002
	^{85}Rb	stable	1.6117e-004	7.0630e+002	4.6600e+003	2.7869e-003	7.0630e+002	4.6600e+003	1.9774e+002	4.6744e+002
2	^{36}Cl	1.10e+08	7.0775e-005	6.6301e+002	4.6200e+003	1.2238e-003	6.6301e+002	4.6200e+003	2.0092e+002	4.5925e+002
	^{129}I	5.73e+09	7.0881e-005	6.6356e+002	4.6200e+003	1.2256e-003	6.6356e+002	4.6200e+003	2.0092e+002	4.5925e+002
3	^{90}Sr	1.06e+04	3.0134e-007	1.3753e+002	4.4600e+003	5.2106e-006	1.3753e+002	4.4600e+003	1.9773e+002	4.5811e+002
	^{90}Y	2.67e+00	7.5922e-011	1.3753e+002	4.4600e+003	1.3128e-009	1.3753e+002	4.4600e+003	1.9773e+002	4.5811e+002
	^{90}Zr	stable	8.5148e-005	6.8548e+002	4.6200e+003	1.4723e-003	6.8548e+002	4.6200e+003	1.9773e+002	4.5811e+002
4	^{99}Tc	7.78e+07	3.2924e-005	6.6740e+002	4.6200e+003	5.6930e-004	6.6740e+002	4.6200e+003	1.9977e+002	4.5616e+002
5	^{137}Cs	1.10e+04	5.4948e-007	1.3205e+002	4.4600e+003	9.5014e-006	1.3205e+002	4.4600e+003	1.9681e+002	4.6115e+002
	^{137}Ba	stable	1.1601e-004	6.7726e+002	4.6200e+003	2.0059e-003	6.7726e+002	4.6200e+003	1.9681e+002	4.6115e+002

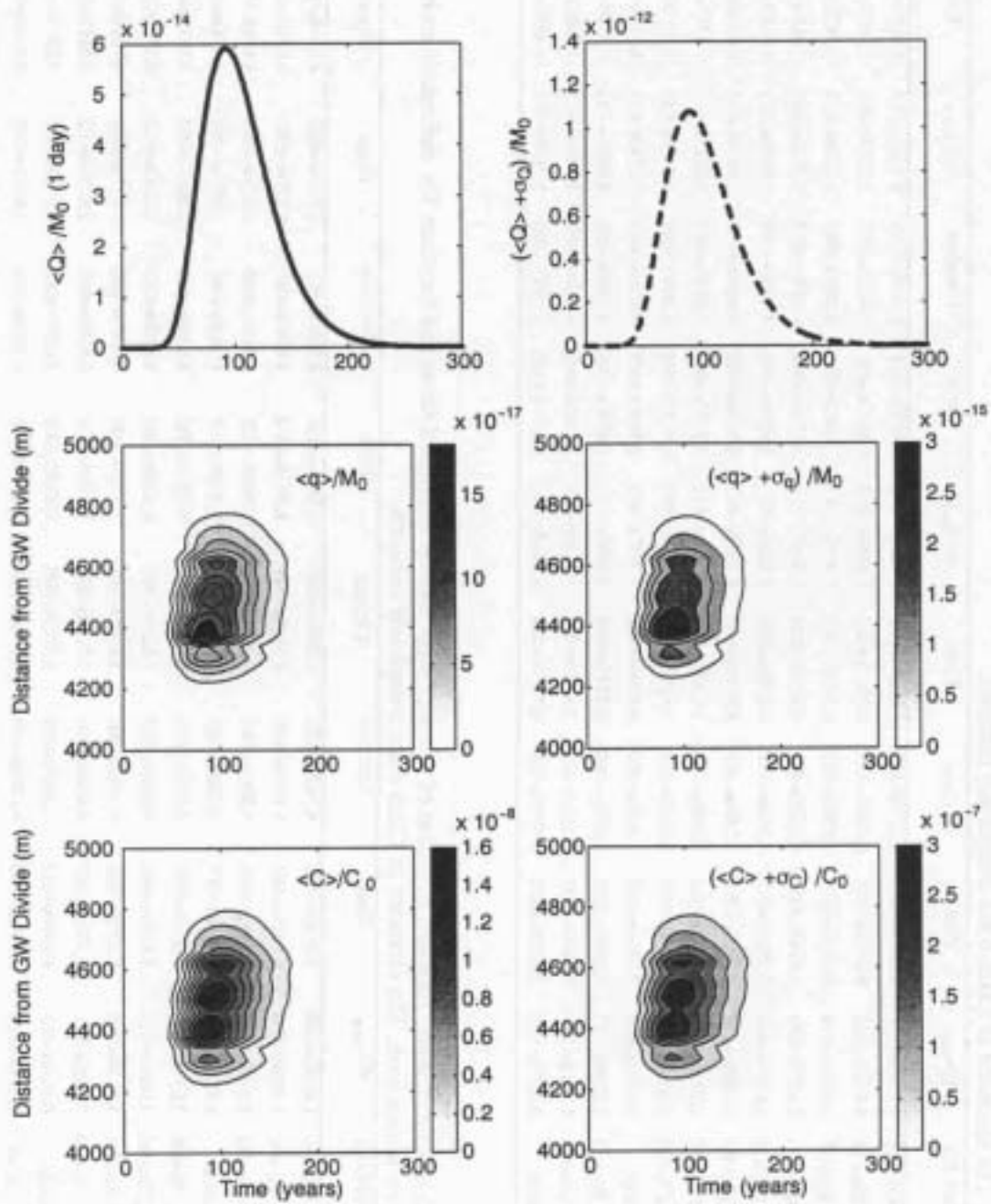


Figure 5.15. Statistics of mass flux and concentrations for ^3H with $\kappa = 0.434$.

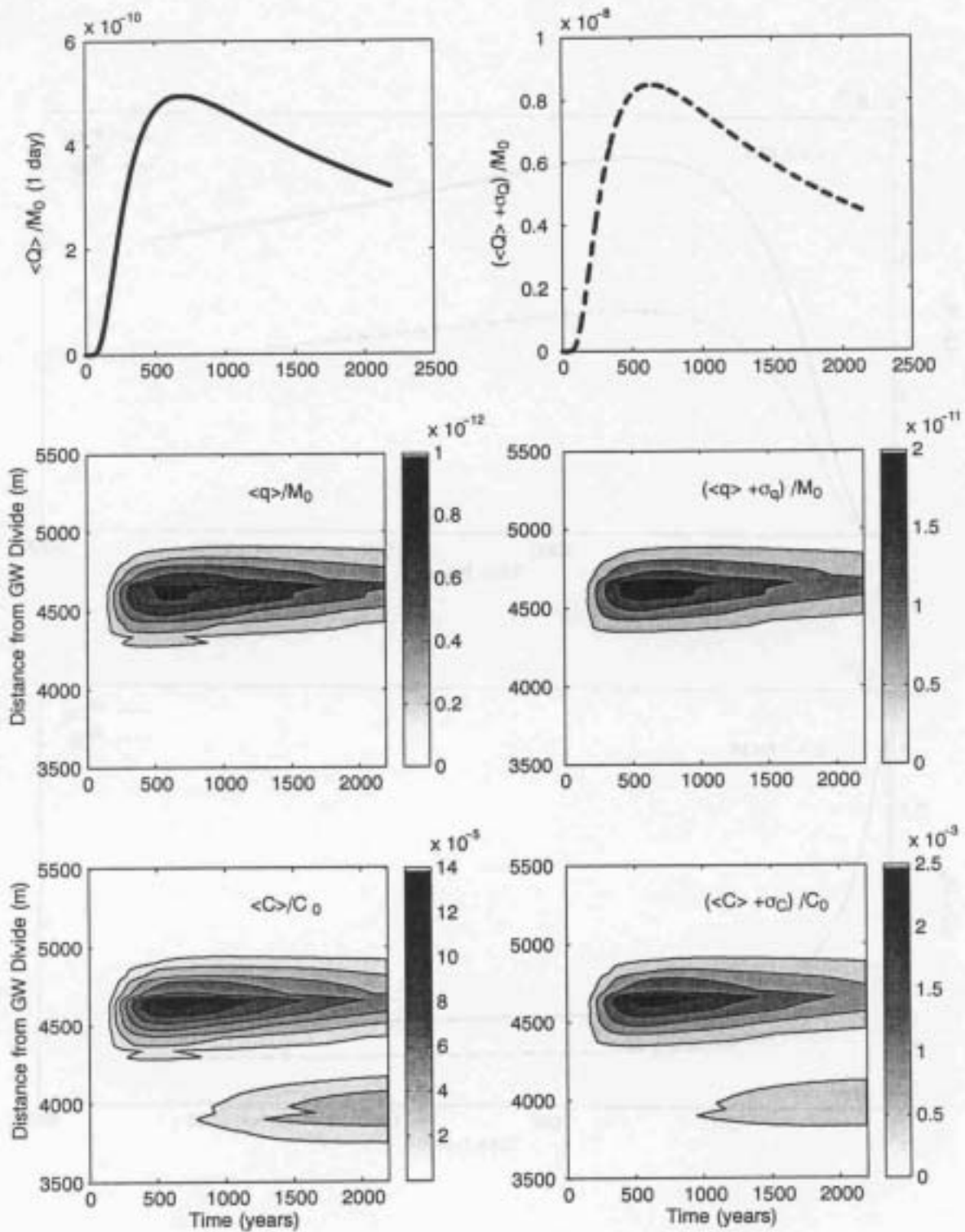


Figure 5.16. Statistics of mass flux and concentrations for ^{14}C with $\kappa = 0.434$.

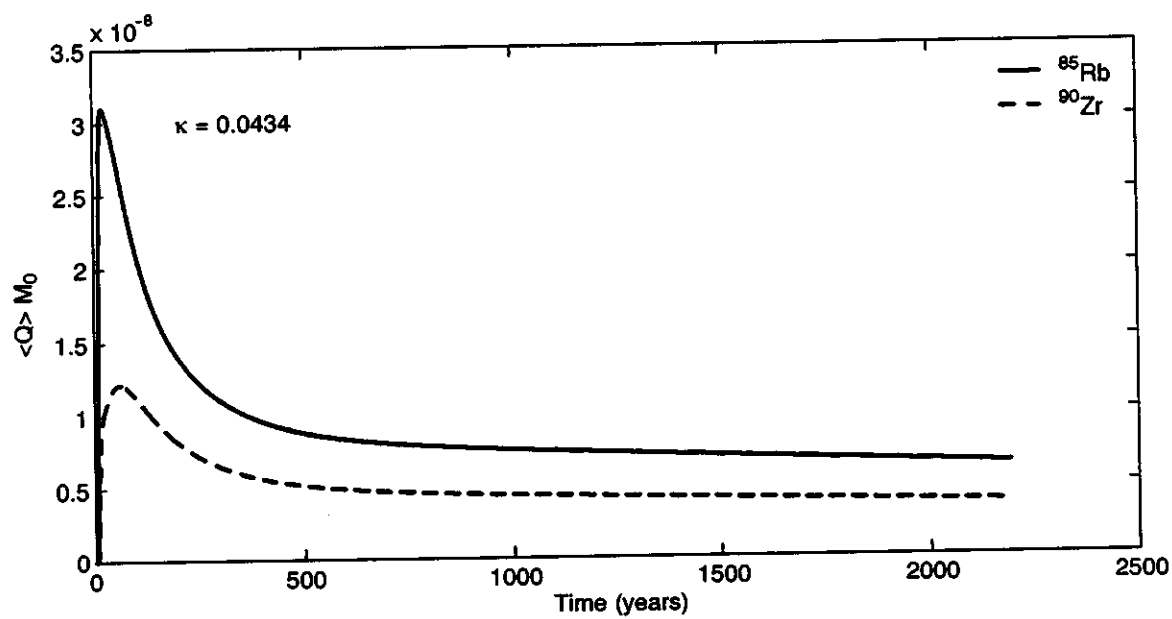
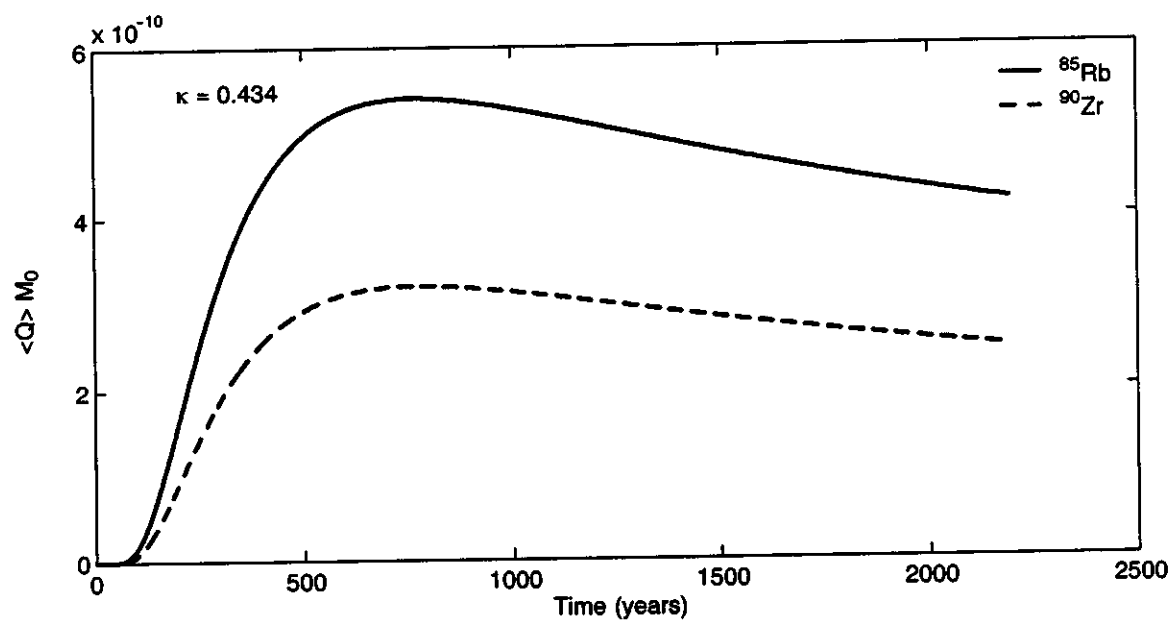


Figure 5.17. The effect of the release category (proportion of glass release) on breakthrough.

5.1.3 Milrow Summary and Discussion

A three-step modeling scheme is adapted for Milrow where a calibration analysis is followed by a multi-parameter sensitivity analysis for many flow and transport parameters, and finally the combined effect of a few random parameters is addressed in the third step of modeling. Data available from the Milrow site are used to identify the location of the transition zone and the vertical distribution of groundwater heads near the test. The existence of these two sets of data constrains the model calibration. Many combinations of the parameters governing the density-driven flow modeling are tested with no single parameter-combination producing results that match the two data sets. A calibration case is then selected and used in the second step which entailed studying the sensitivity of transport results to the uncertainty associated with the flow and transport parameters. The result of this sensitivity analysis is the reduction of the number of uncertain parameters from seven to only three. Uncertainties of recharge, conductivity and fracture porosity are found to have the most significant effect on travel times and transverse locations where the plume hits the seafloor.

Three random distributions are then generated for these parameters and used in the final modeling stage where each realization utilizes randomly generated recharge, conductivity and porosity values. The combined distributions for these three parameters produce a wide range of variability around the base-case mean values. The recharge-conductivity ratio changes by more than one order of magnitude (the maximum ratio is roughly 25 times the minimum ratio). The conductivity-porosity ratio also changes by about three orders of magnitude. This wide range of variability in the input parameters leads to a large degree of variability in arrival time of radionuclides. This arrival time is mainly affected by the conductivity-porosity ratio, which changes significantly between realizations.

The final results show that the radionuclides could start to arrive at the seafloor within 10 years of release from the cavity. However, the distribution of first arrival time covers a very long time scale, extending from 10 years to 2,200 years and beyond. About 8 percent of the total realizations do not show any breakthrough within 2,200 years. The early arrival is mainly controlled by a few realizations in which the transition zone is below the cavity. This allows for the direct and quick migration of radionuclides from the cavity to the seafloor. The important fact is that the portion of mass that arrives early, even if very small, contributes to the peak flux and concentration more than the rest of the mass arriving at a later time due to radioactive decay. This is particularly true for short-lived radionuclides such as ^3H .

As with any radioactive transport simulation, the most influential parameters are those changing the travel time. Uncertainty in estimating such parameters leads to great uncertainty in transport results, which is magnified by the radioactive decay that is a function of the residence time. The analysis performed for Milrow (and the other tests, as will be seen later) reveals the very crucial aspect of selecting the value of the fracture porosity. With lack of data, a very small fracture porosity is used and the porosity value is varied by two orders of magnitude. These choices are very crucial and have critical consequences when it comes to travel times and radioactive decay. Increasing the porosity values by only an order of magnitude may lead to a significant reduction in mass flux and concentrations especially for short-lived nuclides.

The uncertainty associated with determining the hydraulic conductivity value is not as crucial as that of the porosity since a significant amount of conductivity data exists that gives a good idea about the range of conductivity values at the island. Of course, both uncertainties are equally important for travel time, but there are sufficient data to alleviate major concerns about the range of values selected for the hydraulic conductivity, while no data exist for the fracture porosity.

5.2 Long Shot Flow and Transport Results

The calibration process is repeated for Long Shot, with the same objective of selecting base-case flow and saltwater intrusion parameters that provide a modeling result as close to reality as possible. Though Long Shot has the same types of calibration data used at Milrow (chloride concentrations, and deep heads), the quantity of data is smaller. Specifically, the chloride profiles do not extend into the transition zone so they cannot be used to identify the location and width of the transition zone at Long Shot. Similarly, the deep hydraulic head measurements are restricted to shallower depths than at the other sites.

Three random distributions are generated for the conductivity, recharge and fracture porosity. Distributions with 500 values of conductivity and recharge are generated. An upper and a lower limit for the recharge-conductivity ratio are specified to ensure that the transition zone is consistent with the available data and information at Long Shot and the other sites. The thickness of the freshwater lens is considered possibly larger than that at Milrow, based on limited information at Cannikin, suggesting that the freshwater lens is asymmetric between the Bering and Pacific sides of the island (Fenske, 1972). Therefore, the 500 values for the recharge conductivity ratio are computed and the realizations that satisfy the condition $0.0047 \leq \text{Rech}/K \leq 0.019$ are selected, which yielded 240 realizations of the random values. It should be mentioned that the lower limit is about four times the one used for Milrow but the upper limit is smaller (0.0347 for Milrow). This is to eliminate those realizations with very shallow transition zones, which are unlikely to occur at Long Shot. The minimum, mean and maximum values of K are 2.3×10^{-3} , 1.21×10^{-2} , and 4.44×10^{-2} m/day, respectively. For the recharge, these limits are 0.809, 3.416, and 14.09 cm/year, respectively. Independently of these values, 240 random porosity values are generated with a minimum of 1.024×10^{-5} , a mean of 4.11×10^{-4} , and a maximum of 5.2×10^{-3} . Figure 5.18 displays the histograms of these three distributions. In comparing these distributions to those used in Milrow, it is found that recharge has a higher mean but conductivity has a lower mean. This is to be expected, as it is an attempt to reproduce a deeper transition zone as compared to Milrow. Porosity values, on the other hand, show a similar distribution as for Milrow.

Figure 5.19 compares the recharge-conductivity ratio and the conductivity-porosity ratio for the generated distributions to the base-case values. Recall that in the base case, $K = 1.58 \times 10^{-2}$ m/day, $\text{Rech} = 3.65$ cm/year, and $\theta = 5.0 \times 10^{-4}$. The plots in Figure 5.19 illustrate how the two ratios (Rech/K and K/θ) vary among the 240 realizations around the base-case ratios. As can be seen in the figure, Rech/K varies from a minimum that is about 0.7 times the base-case ratio to a maximum that is about three times larger. More realizations lie above the base-case line than below it, which indicates some skewness towards the high recharge range that is necessary to drive the transition zone downwards. The conductivity-porosity ratio varies from ten times smaller to about 50 times

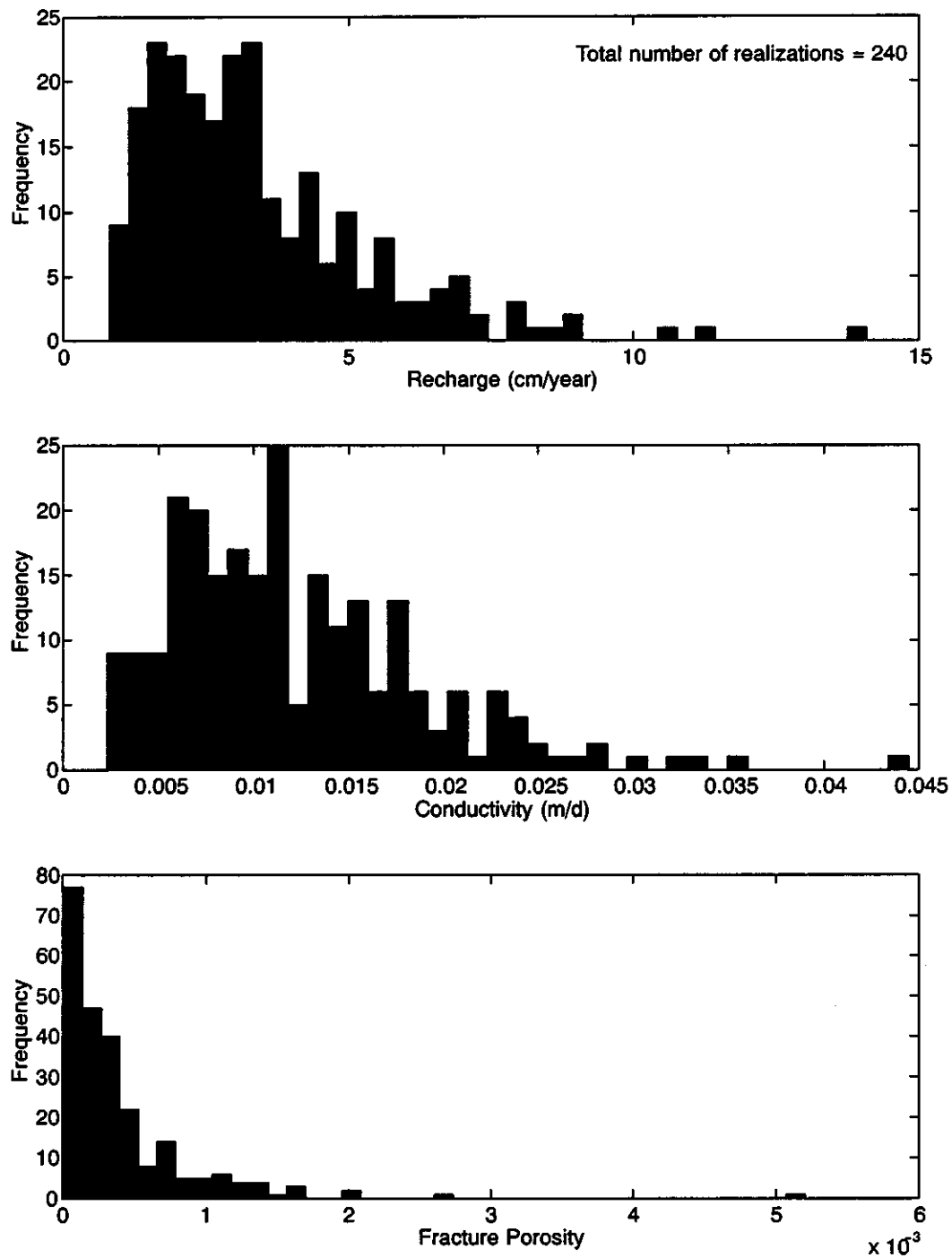


Figure 5.18. Randomly generated distributions for *Rech*, *K* and θ in the second (final) modeling stage.

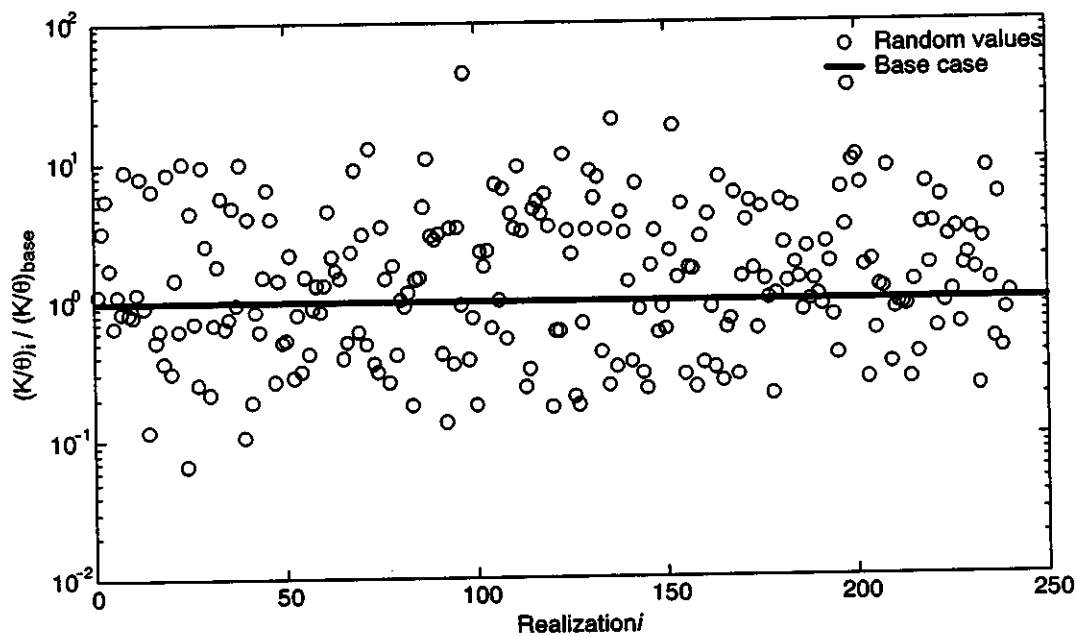
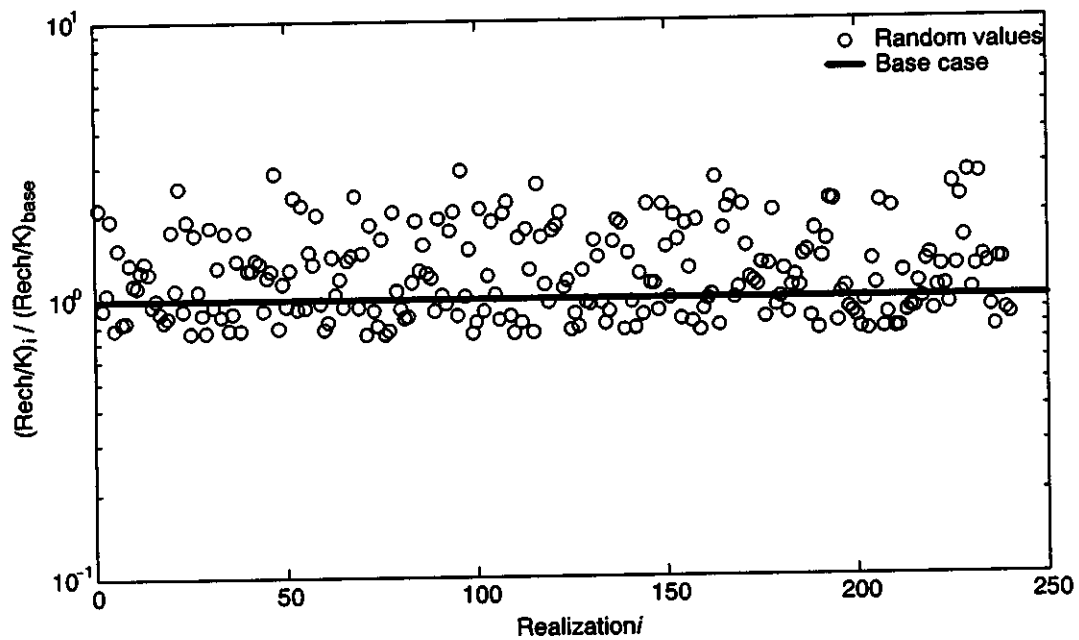


Figure 5.19. Comparison of the randomly generated recharge-conductivity and conductivity-porosity ratios relative to the base-case values.

larger than the base-case value. This ratio is more or less evenly distributed around the base-case value. The flow and transport parameters used for Long Shot are summarized in Table 5.4.

Table 5.4. Parameter range for Long Shot simulations.

Parameter	Minimum	Mean	Maximum	σ	Distribution
K	2.3×10^{-3}	1.21×10^{-2}	4.44×10^{-2}	6.66×10^{-3}	~ lognormal
$Rech$	0.809	3.416	14.09	2.01	~ lognormal
θ	1.024×10^{-5}	4.11×10^{-4}	5.2×10^{-3}	5.19×10^{-4}	~ lognormal
A_L	-	100	-	-	-
A_T	-	10	-	-	-
α_L	-	5.0	-	-	-
α_T	-	0.5	-	-	-
κ	-	0.434	-	-	-
K_g	-	1.26×10^{-7}	-	-	-

FEFLOW is used to solve the density-driven flow problem for 240 realizations with the recharge, conductivity, and porosity values already generated. Macrodispersivity values are fixed at 100 m and 10 m in the longitudinal and transverse directions, respectively. Domain geometry and boundary conditions remain unchanged as compared to the analysis in Section 4. To assess the choice of the combined random values used in this analysis, the results of these realizations at location EH-5 are analyzed and compared to the measured heads and concentrations. Figure 5.20 illustrates this comparison. In addition to the data points, the mean of the 240 realizations, the mean \pm one standard deviation, and the base-case result are plotted. The variabilities in the input parameters resulted in a mean concentration profile that reasonably matches the concentration data, though slightly underpredicting the salinity observed above the transition zone. The head data are well bounded by the one standard deviation interval. The mean of MC realizations provides higher heads than indicated by the data, but similar gradients.

Radionuclide transport simulations are also performed in a manner similar to Milrow. All transport parameters are kept constant in all realizations. Glass dissolution rate, k_g , is taken as $1.26 \times 10^{-7} \text{ day}^{-1}$, local dispersivities are fixed at 5.0 and 0.5 m, and the matrix diffusion parameter is 0.434, as discussed earlier. The particle-tracking simulations are performed for the six cases shown in Table 5.5 with different time steps than used in Milrow. This is due to the fact that the Long Shot cavity is very shallow as compared to Milrow, and as such, particles released in the cavity experience the high velocity region in the freshwater lens above the transition zone for many of the realizations considered. The selection of the time step size for the three sites is determined by analyzing the velocity magnitude at the seepage face for all individual realizations. The maximum value of the velocity at the seepage face is determined for each realization and then the absolute maximum of all these maxima is used to compute the time step such that when multiplied together, they result in a step size smaller than the grid size (100 m). The non-decayed transport results are discussed first, followed by the final decayed results for a selected number of radionuclides.

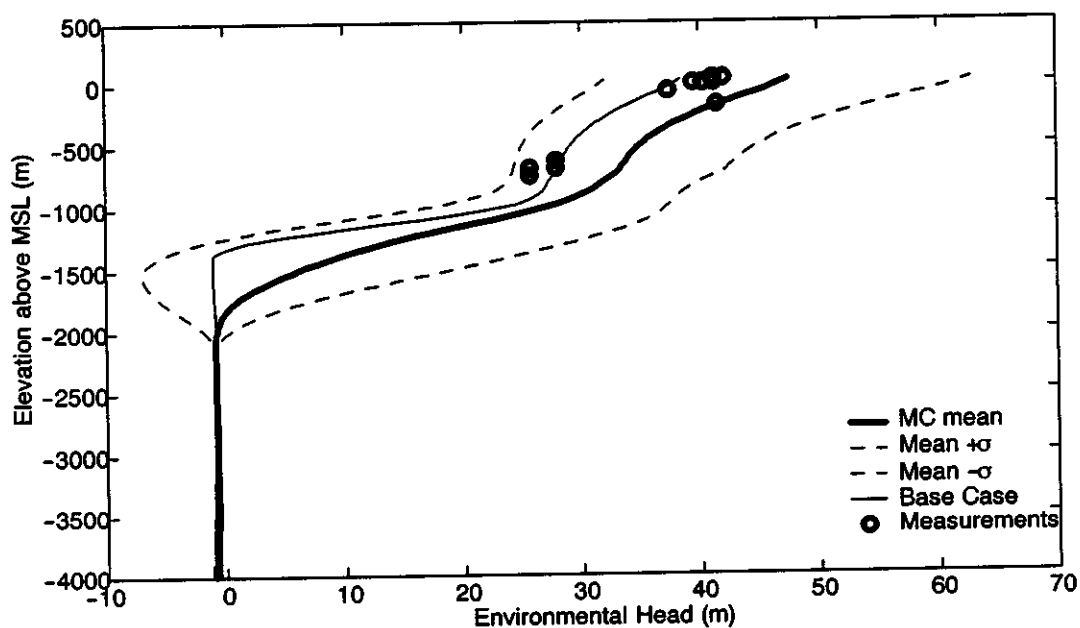
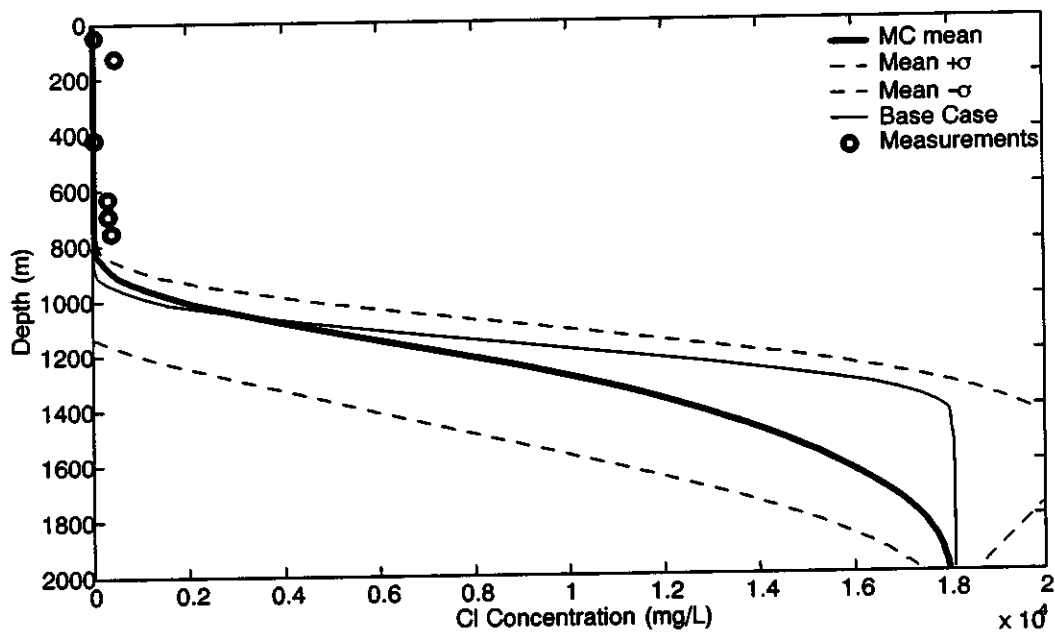


Figure 5.20. Sensitivity of modeled heads and concentrations to the combined uncertainties of $Rech$, K and θ in the second modeling stage at Long Shot.

Table 5.5 Values of parameters specific to individual solute classes.

Parameter	Case 1	Case 2	Case 3	Case 4	Case 5	Case 6
Total Time, t (years)	2,191	2,191	2,191	2,191	2,191	4,382
Time Step, Δt (days)	25	25	25	25	25	50
Release Ratio (%), Hydraulic Release / Geochemical Release	100/0	50/50	60/40	20/80	80/20	5/95
Retardation Factor	1	1	1	1	1	1.8
Geochemical Release Coefficient k_r (day ⁻¹)	NA	1.26×10^{-7}	1.26×10^{-7}	1.26×10^{-7}	1.26×10^{-7}	1.26×10^{-7}

5.2.1 Undecayed Transport Results

The results of the first arrival time and the location and depth of the breakthrough are analyzed for the first class with 100 percent hydraulic release and no retardation. Also, no matrix diffusion or decay computations are included in this analysis unless stated otherwise. Similar to the analysis of Milrow, the 240 realizations are analyzed in terms of the percentage of mass that breaks through within 2,200 years, the first and last arrival times, the duration of breakthrough, the location of the plume edges with respect to the bathymetric profile, the plume width and the depths below MSL where breakthrough occurs. Since the Long Shot cavity is very shallow as compared to the other two tests, almost all realizations show 100 percent mass breakthrough within 2,200 years. Only six realizations out of 240 show less than 95 percent but greater than 85 percent mass breakthrough within this time frame.

Figure 5.21 displays the distributions of the first arrival time (whether it is for one particle or a thousand particles), the last arrival time and the duration of breakthrough. The figure shows that about 55 realizations (out of 240) show a first mass arrival within 10 years. Most of the realizations show a first arrival time less than 300 years. The figure also shows that about 45 realizations require a last arrival time beyond 2,200 years. Many of these realizations have about 99 percent of the mass arriving at the seafloor within the simulation time and the remaining one percent in the simulation domain is what requires the last arrival to be beyond the 2,200-year simulation time. Figure 5.22 displays the distributions of the locations of the plume edges on the bathymetric profile, the plume width, and the distance from the groundwater divide to the center of the plume that is obtained after accounting for matrix diffusion effect. The location of the left (first) edge of the plume is concentrated between 2,800 m and 3,600 m from the island centerline, while the right (second) edge of the plume is located within the range of 3,600 m to 5,500 m. The location of the right edge of the plume shows more spread than the left edge. Comparing these results to those of Milrow reveals that the breakthrough at Long Shot is spread over a shorter length than at Milrow. One reason for this result is the fact that the initial source size (cavity) at Long Shot is much smaller than the Milrow cavity (and also much smaller than at Cannikin). The Long Shot cavity is about 122 x 122 m, whereas Milrow and Cannikin have 212 x 212 m and 354 x 354 m, respectively. In addition to the cavity size, the location of the cavity relative to the varying transition zone location plays a significant role in

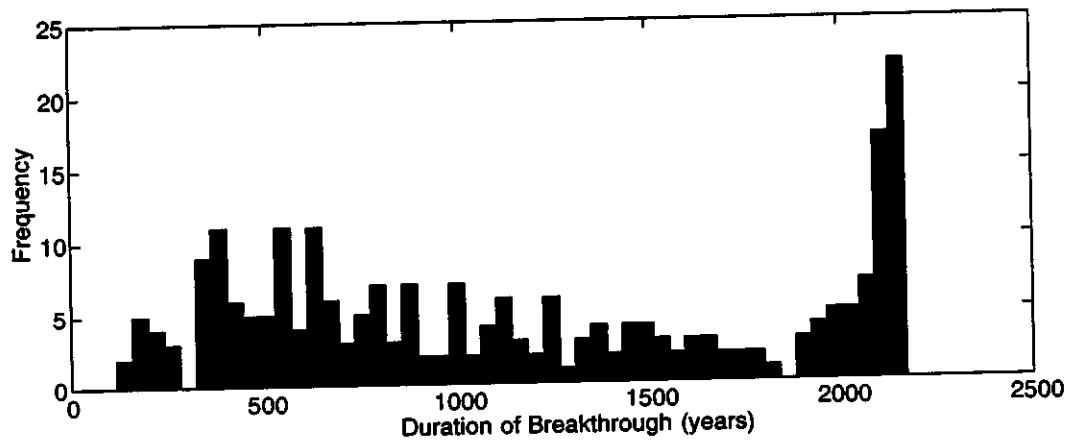
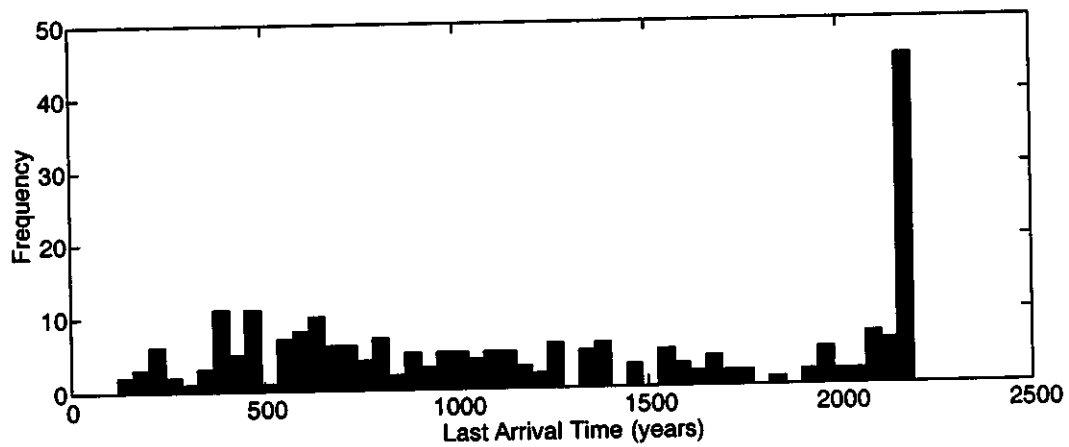
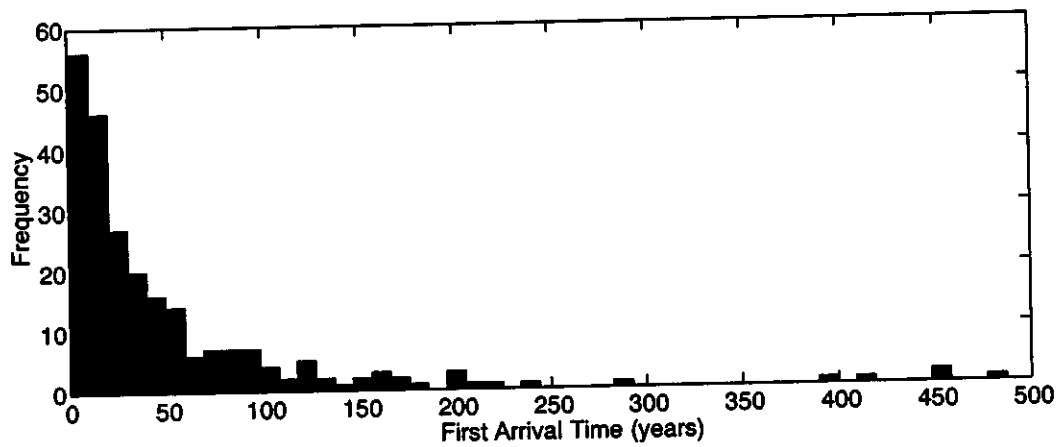


Figure 5.21. Histograms showing the distribution of first arrival time, last arrival time, and duration of breakthrough for Long Shot.

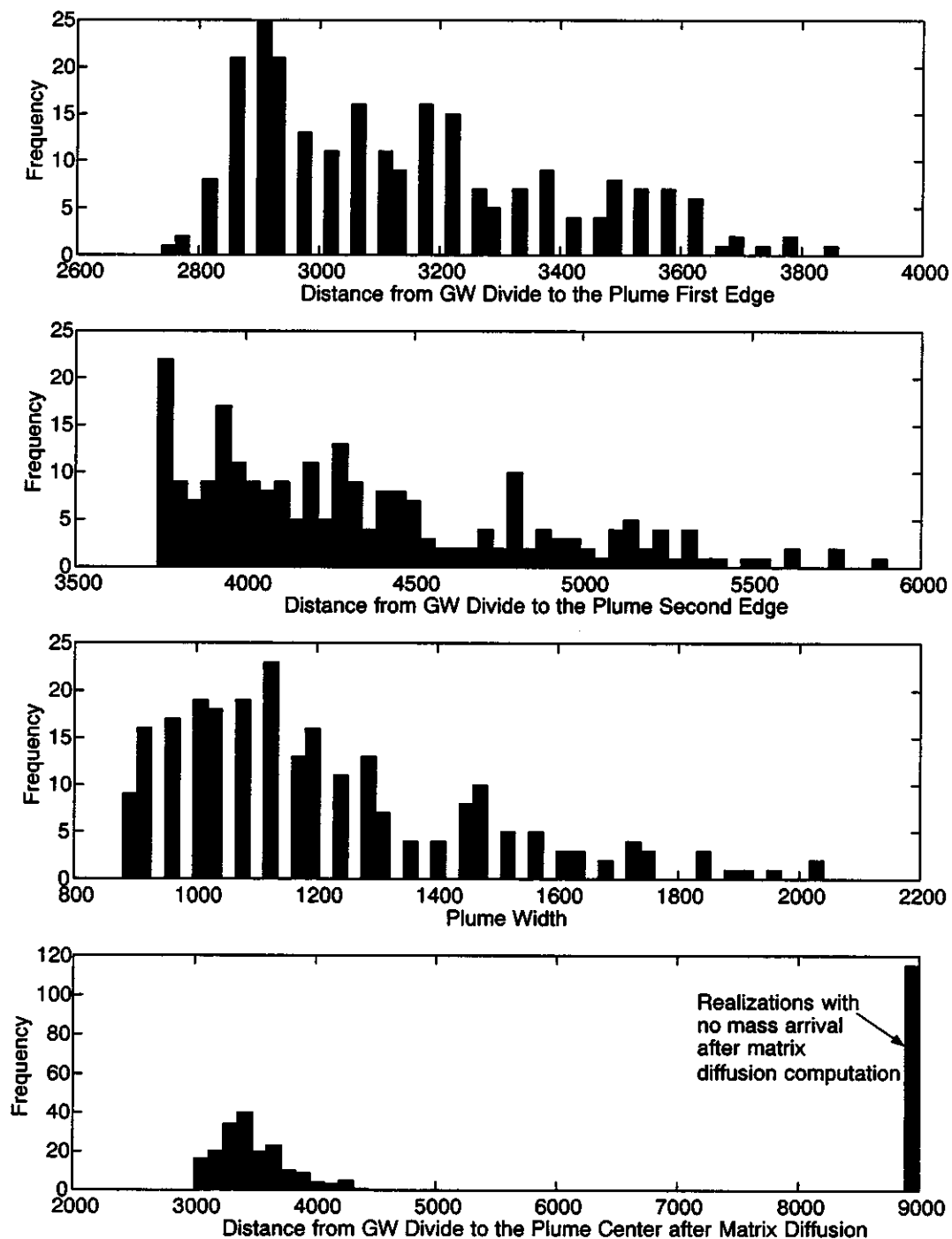


Figure 5.22. Histograms showing the distance from groundwater divide to plume edges and plume width for Long Shot.

transport results. The Long Shot cavity is always located at the fresh water lens and as such the radionuclides have a uniform path towards the seepage face in almost all realizations.

In addition to the location of the plume edges, Figure 5.22 also shows that the plume is much wider than at Milrow. The plume width varies between 900 m to about 2,000 m with many realizations having the width between 900 and 1,300 m. At Milrow, the plume had a width mainly less than 1,000 m. This can be attributed to the fact that at Milrow, many realizations showed a very small percentage of mass arriving at the seafloor, which breaks through within a narrow length along the bathymetric profile leading to the small plume width as compared to Long Shot, where all realizations show above 85 percent mass breakthrough. The last quantity in Figure 5.24 is the distance from the divide to the plume center. When accounting for matrix diffusion, about 117 realizations (out of 240) did not contribute to the final breakthrough results at Long Shot. This number is to be compared to 240 (out of 300) at Milrow. These realizations have late arrival and slow groundwater velocities, which increase the residence time of the mass in the fractured system and allow for more diffusion into the matrix as opposed to the realizations with early arrival and high velocities.

Figure 5.23 shows the distribution of the depth below MSL of the plume edges where breakthrough occurs. This information is very important for risk assessment studies as it helps determine the nature of the currents that disperse the flowing mass and the type of sea creatures living at these depths. The figure shows that the left edge of the plume exists at a depth of 20 to 40 m, whereas the right edge exists at a depth of 40 to 80 m below MSL. Breakthrough at Milrow occurs at depths ranging from 2 m to about 25 m. The deeper locations at Long Shot are a result of the different bathymetric profile as compared to Milrow, Figure 2.9.

5.2.2 Transport Results with Radioactive Decay

For all 12 radionuclides representing the first five cases, the results are tabulated in Table 5.6. No breakthrough occurred for radionuclides in Case 6 (though the sensitivity analysis of the matrix diffusion parameter did result in breakthrough for Case 6, as discussed later in Section 6). The structure of the table is similar to that of Table 5.3 presented earlier for Milrow. Figure 5.24 depicts the flux and concentration results for tritium, ^3H , which is an element in Case 1, with a matrix diffusion parameter value of 0.434. The normalized mean concentration distribution has a peak value of about 1.8×10^{-4} , which is the highest value among the three tests. Recall that this value for Milrow was 1.6×10^{-8} . Adding one standard deviation to the Long Shot value leads to a normalized ^3H peak mean concentration of about 2.5×10^{-3} . This peak occurs roughly at 25 to 30 years after the test and at about 3,500 m from the island center (about 1,370 m from the shoreline). These normalized concentrations are about four orders of magnitude larger than the result at Milrow. The arrival time at Long Shot is 40 to 75 years earlier than Milrow. This is to be expected, as the shallow cavity location leads to shorter travel distances to the seepage face. Furthermore, the location of the cavity within the freshwater lens with very high velocities leads to shorter travel times as compared to Milrow. The results for ^{14}C , shown in Figure 5.25, show that the mass flux and peak concentration are about an order of magnitude higher than those of ^3H with $\kappa = 0.434$. The normalized peak of

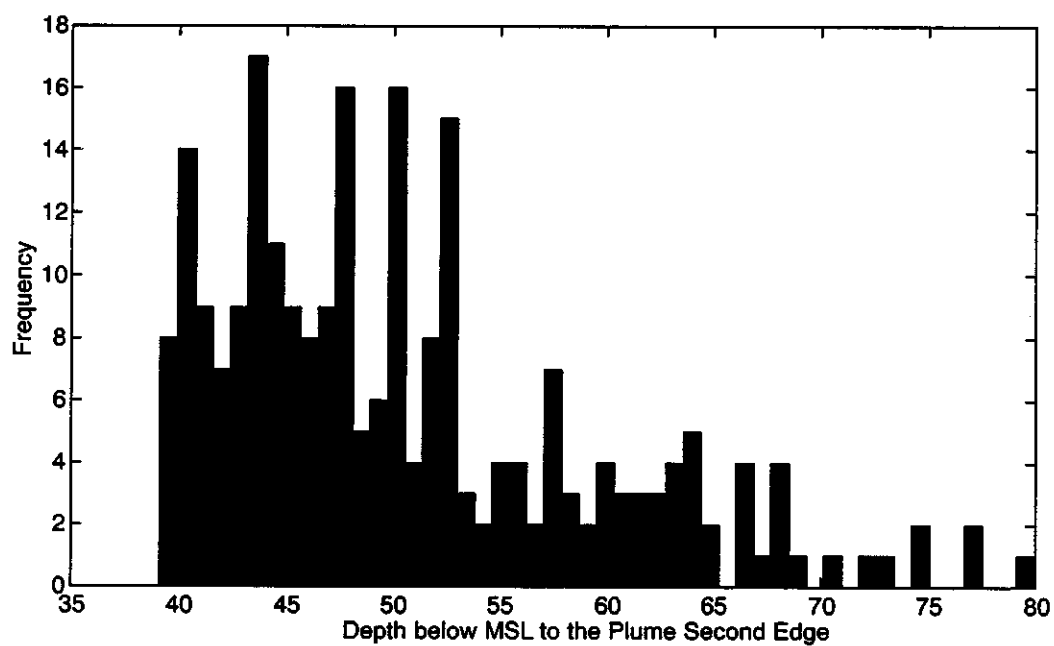
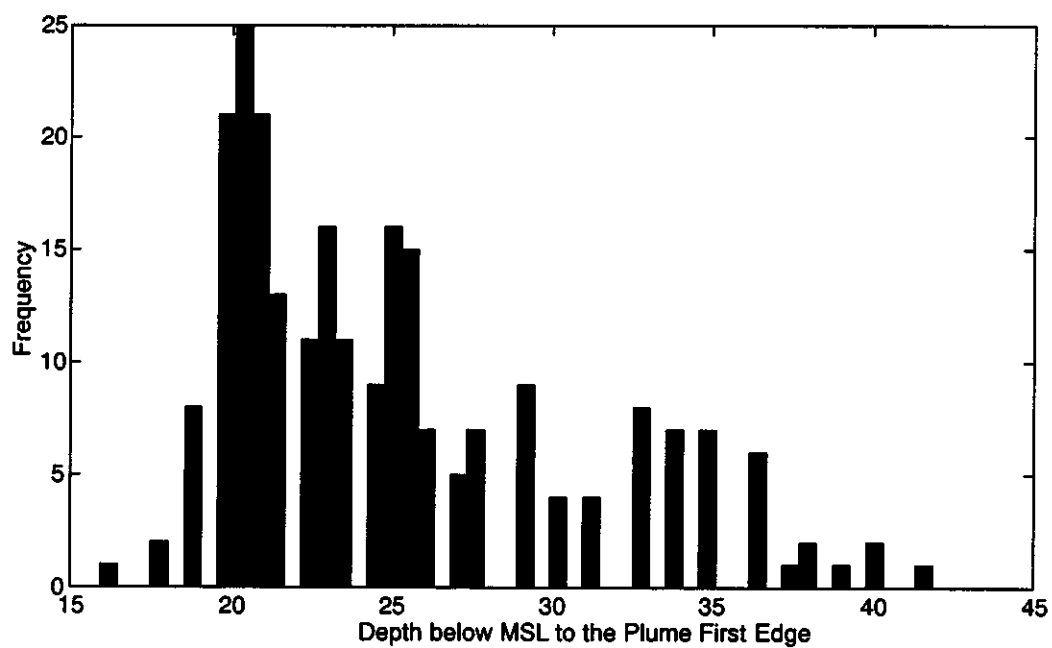


Figure 5.23. Histograms showing the distributions of depths below MSL at which the plume edges discharge to the ocean floor for Long Shot.

Table 5.6a. Peaks of expected and standard deviation of mass flux and the associated times and locations for radionuclides in the Long Shot source term. The elements in Class 6 are completely decayed.

Case	Radio-nuclide	Half-life	$\langle Q \rangle_{\max}$	Time	$\langle \sigma Q \rangle_{\max}$	Time	$\langle q \rangle_{\max}$	Time	Location	$(q)_{\max}$	Time	Location
1	^3H	4.49e+03	2.2819e-009	3.1781e+001	2.1255e-008	2.9041e+001	5.7314e-012	2.8493e+001	3.5000e+003	6.7322e-011	2.7397e+001	3.5000e+003
	^{14}C	2.09e+06	4.5037e-008	1.9836e+002	2.6974e-007	1.0685e+002	6.8559e-011	1.0795e+002	3.5800e+003	6.3165e-010	8.5479e+001	3.5800e+003
	^{85}Kr	3.91e+03	1.7695e-009	2.9589e+001	1.6841e-008	2.6849e+001	4.5505e-012	2.6849e+001	3.5000e+003	5.3802e-011	2.6301e+001	3.5000e+003
	^{85}Rb	stable	4.6171e-008	2.1315e+002	2.7303e-007	1.0904e+002	6.9416e-011	1.1123e+002	3.5800e+003	6.3598e-010	8.8219e+001	3.5800e+003
2	^{36}Cl	1.10e+08	2.2992e-008	2.1260e+002	1.3593e-007	1.0904e+002	3.3522e-011	1.1342e+002	3.5800e+003	3.0983e-010	8.8767e+001	3.5800e+003
	^{129}I	5.73e+09	2.3003e-008	2.1260e+002	1.3596e-007	1.0904e+002	3.3531e-011	1.1342e+002	3.5800e+003	3.0989e-010	8.8767e+001	3.5800e+003
3	^{90}Sr	1.06e+04	7.8061e-009	4.7123e+001	6.4799e-008	4.2192e+001	1.6773e-011	4.1644e+001	3.5400e+003	1.8979e-010	3.7808e+001	3.5000e+003
	^{90}Y	2.67e+00	1.9668e-012	4.7123e+001	1.6326e-011	4.2192e+001	4.2260e-015	4.1644e+001	3.5400e+003	4.7817e-014	3.7808e+001	3.5000e+003
	^{90}Zr	stable	4.5933e-008	2.2849e+002	2.5782e-007	1.3151e+002	6.6001e-011	1.4027e+002	3.5800e+003	5.7582e-010	1.0849e+002	3.5800e+003
4	^{99}Tc	7.78e+07	9.2846e-009	2.1370e+002	5.5027e-008	1.0849e+002	1.4187e-011	1.0466e+002	3.5800e+003	1.3198e-010	8.4932e+001	3.5800e+003
5	^{137}Cs	1.10e+04	6.4987e-009	4.8219e+001	5.3695e-008	4.3288e+001	1.3979e-011	4.3836e+001	3.5800e+003	1.4522e-010	4.2192e+001	3.5800e+003
	^{137}Ba	stable	3.6911e-008	2.2959e+002	2.0645e-007	1.3370e+002	5.3348e-011	1.4356e+002	3.6200e+003	4.6512e-010	1.0849e+002	3.5800e+003

Table 5.6b. Peaks of expected and standard deviation of concentration and the associated times and locations for radionuclides in the Long Shot source term. The elements in Class 6 are completely decayed.

Case	Radio-nuclide	Half-life	$\langle C \rangle_{\max}$	Time	Location	$\langle \sigma C \rangle_{\max}$	Time	Location	σ_{Time}	σ_{Location}
1	^3H	4.49e+03	1.9868e-004	2.7945e+001	3.5000e+003	2.6769e-003	2.7397e+001	3.5000e+003	3.4894e+002	2.8975e+002
	^{14}C	2.09e+06	2.0276e-003	1.0137e+002	3.5800e+003	2.3295e-002	7.0137e+001	3.5000e+003	3.4894e+002	2.8975e+002
	^{85}Kr	3.91e+03	1.5845e-004	2.6301e+001	3.5000e+003	2.1456e-003	2.5753e+001	3.5000e+003	3.4894e+002	2.8975e+002
	^{85}Rb	stable	2.0503e-003	1.0411e+002	3.5800e+003	2.3276e-002	7.3973e+001	3.5000e+003	3.4894e+002	2.8975e+002
2	^{36}Cl	1.10e+08	1.0050e-003	9.9726e+001	3.5400e+003	1.1304e-002	7.6712e+001	3.5400e+003	3.5029e+002	2.8866e+002
	^{129}I	5.73e+09	1.0052e-003	9.9726e+001	3.5400e+003	1.1306e-002	7.6712e+001	3.5400e+003	3.5029e+002	2.8866e+002
3	^{90}Sr	1.06e+04	5.6925e-004	3.8904e+001	3.5000e+003	7.4415e-003	3.7260e+001	3.5000e+003	3.4880e+002	2.8975e+002
	^{90}Y	2.67e+00	1.4342e-007	3.8904e+001	3.5000e+003	1.8749e-006	3.7260e+001	3.5000e+003	3.4880e+002	2.8975e+002
	^{90}Zr	stable	1.9266e-003	1.3041e+002	3.5800e+003	2.0241e-002	9.5342e+001	3.5000e+003	3.4880e+002	2.8975e+002
4	^{99}Tc	7.78e+07	4.1982e-004	1.1178e+002	3.6200e+003	4.7040e-003	7.6712e+001	3.5400e+003	3.5106e+002	2.8289e+002
5	^{137}Cs	1.10e+04	4.3458e-004	4.1644e+001	3.5400e+003	5.4721e-003	4.0000e+001	3.5400e+003	3.5032e+002	2.8985e+002
	^{137}Ba	stable	1.5761e-003	1.3425e+002	3.6200e+003	1.5954e-002	1.0356e+002	3.5400e+003	3.5032e+002	2.8985e+002

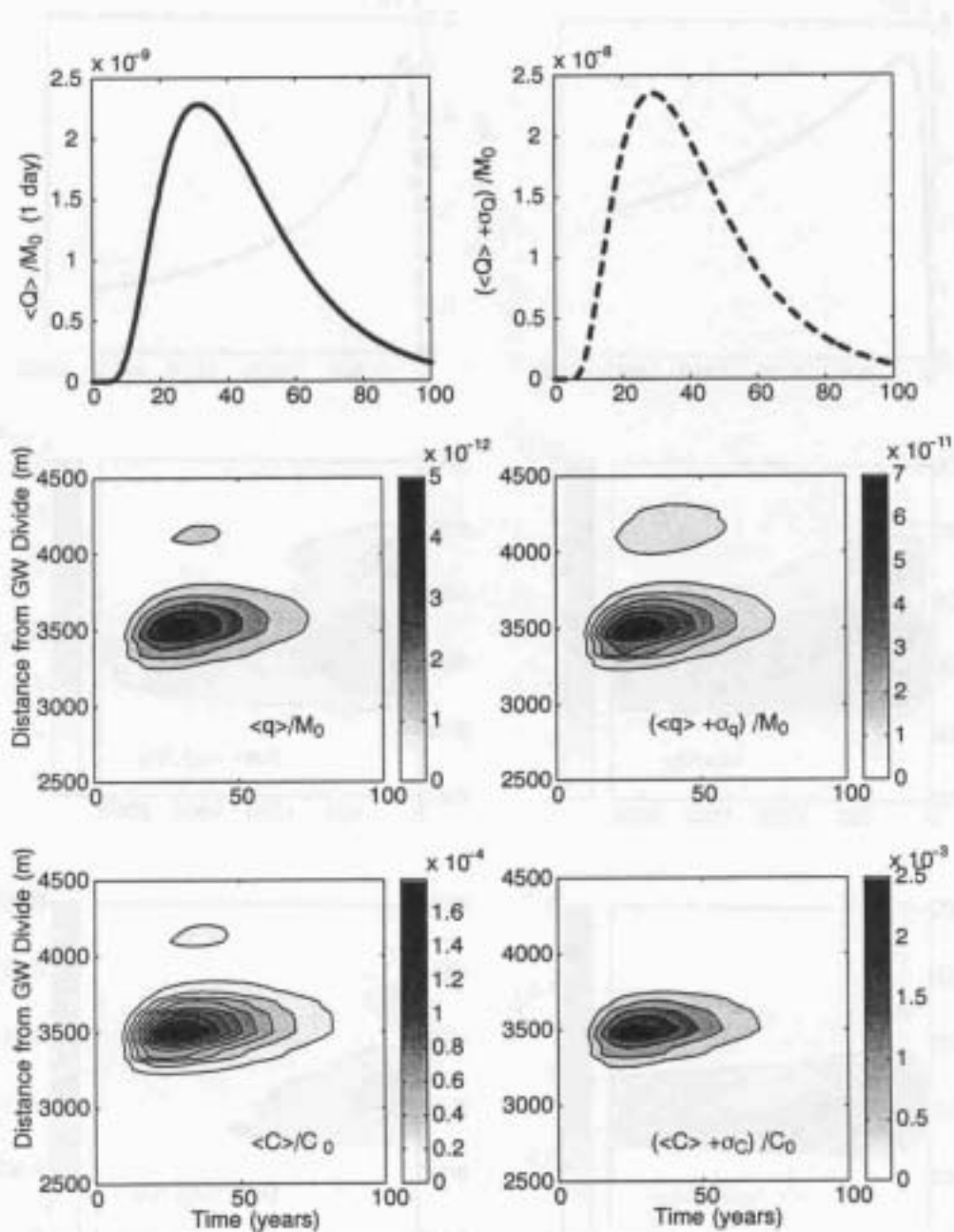


Figure 5.24. Statistics of mass flux and concentration for ^3H from Long Shot with $\kappa = 0.434$.

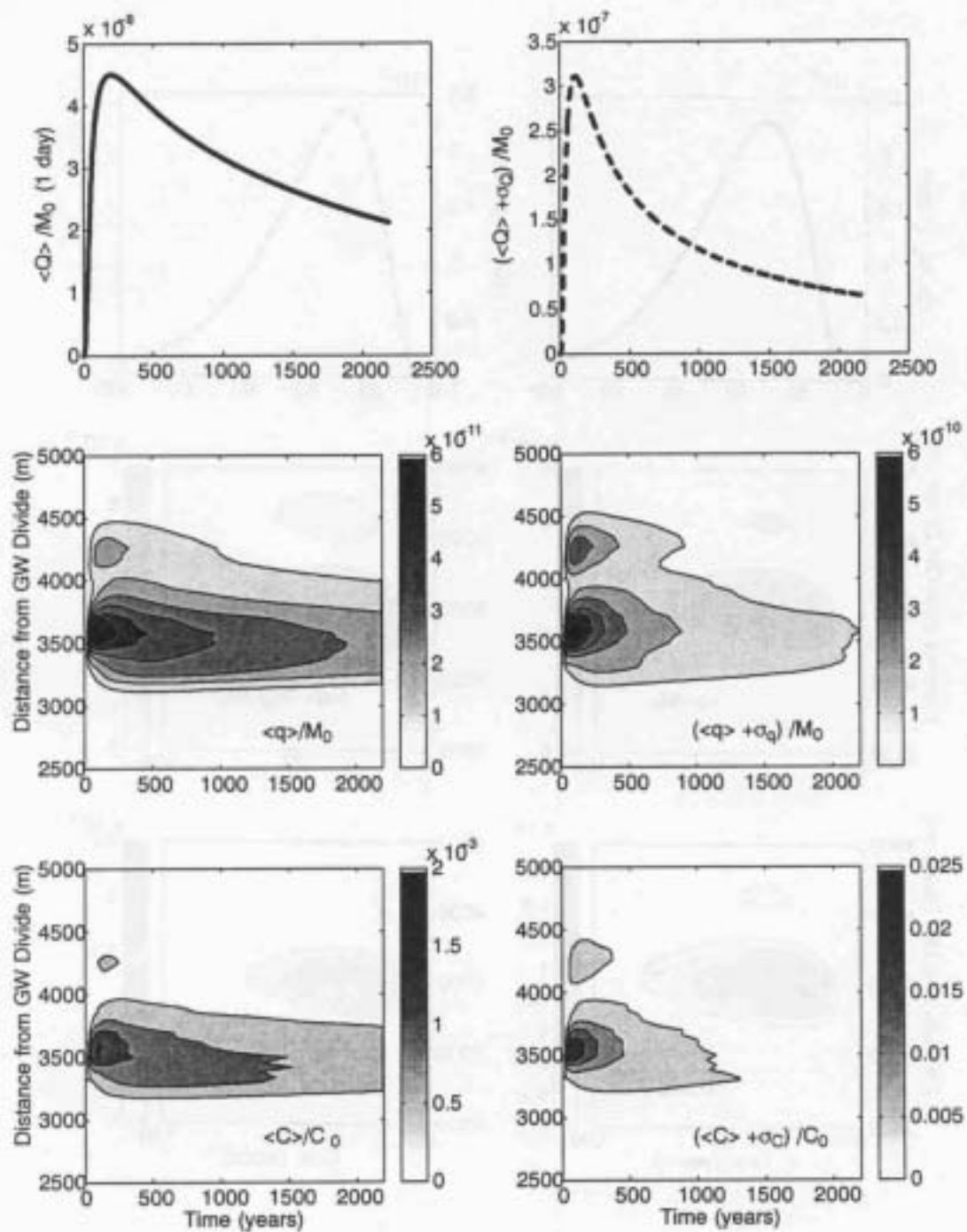


Figure 5.25. Statistics of mass flux and concentration for ^{14}C from Long Shot with $\kappa = 0.434$.

the mean concentration is found to be about 2.0×10^{-3} , and occurs at about 100 years and at 3,500 m from the groundwater divide.

5.2.3 Long Shot Summary and Discussion

The numerical modeling for groundwater flow and radionuclide movement at Long Shot is performed in two stages: a calibration stage and a final modeling stage. The calibration utilized chloride concentration data from one well (EH-5) and head data from a number of wells clustered around the working point of Long Shot. As the quality of the chemical data was questionable due to possible mixing with drilling fluids, a close match to the head data was the target regardless of how the simulated concentrations compare to the measurements. The flow model was successfully calibrated using higher recharge and conductivity than used at Milrow. Calibration indicated that the heads at Long Shot are higher than at Milrow. In addition, the random distributions generated for the final modeling stage were different than Milrow. The final modeling resulted in a confidence interval around the mean that encompasses all head data and part of the concentration data.

The main feature that distinguishes Long Shot from Milrow (and Cannikin) is the location of the cavity, which is very shallow in comparison. Due to this shallow location, all the generated flow realizations encountered a transition zone that lies below the cavity. Therefore, the cavity is always located within the freshwater lens and radionuclide migration occurs through the recharge water moving down and along the transition zone towards the seafloor. This resulted in a 100 percent breakthrough for about 90 percent of the realizations within the selected time frame. The cavity location also has the implication that the travel distances from the test to the seafloor are much smaller than in the other two tests and as such, breakthrough occurs earlier with higher mass fluxes and concentrations. Mean concentrations are, in general, one to a couple of orders of magnitude higher than the other two tests depending on the radionuclide's half-life.

5.3 Cannikin Flow and Transport Results

Three random distributions are generated for the conductivity, recharge and fracture porosity. Distributions with 500 values of conductivity and recharge are generated. An upper and a lower limit for the recharge-conductivity ratio are specified to ensure that the transition zone is within the depths that are thought to encompass the transition zone. The thickness of the freshwater lens is considered much larger than that at Milrow. Therefore, 500 random K values and a similar number for $Rech$ are generated with no correlation among the generated values. The cases that satisfy the condition $0.0047 \leq Rech/K \leq 0.0349$ are selected, which yielded 260 realizations of the random values. These limits are chosen based on the individual results of the location of the transition zone relative to the chloride concentration data. It should be mentioned that the lower limit is about four times the one used for Milrow but the upper limit is the same. The minimum, mean and maximum values of K are 2.17×10^{-3} , 1.19×10^{-2} , and 4.44×10^{-2} m/day, respectively. For the recharge, these limits are 0.809, 3.62, and 18.89 cm/year, respectively. Independently of these values, 260 random porosity values are generated with a minimum of 1.0×10^{-5} , a mean of 4.31×10^{-4} , and a maximum of 5.2×10^{-3} .

Table 5.7 summarizes these values as well as the standard deviation and the type of the distribution used to generate the parameter values. Figure 5.26 displays the histograms of these three distributions. In comparing these distributions to those used in Milrow, it is found that recharge has a higher mean but conductivity has a lower mean. Also, the Cannikin recharge mean is slightly higher than Long Shot, and the conductivity mean is slightly lower than at Long Shot. This is done as an attempt to reproduce a deeper transition zone as compared to Milrow and Long Shot. Porosity values, on the other hand, show a similar distribution as for the other two sites.

Table 5.7. Parameter range for Cannikin flow and transport simulations.

Parameter	Minimum	Mean	Maximum	σ	Distribution
K	2.17×10^{-3}	1.19×10^{-2}	4.44×10^{-2}	6.65×10^{-3}	\sim lognormal
$Rech$	0.808	3.62	18.89	2.32	\sim lognormal
θ	1.0×10^{-5}	4.31×10^{-4}	5.2×10^{-3}	5.4×10^{-4}	\sim lognormal
A_L	-	100	-	-	-
A_T	-	10	-	-	-
α_L	-	5.0	-	-	-
α_T	-	0.5	-	-	-
κ	-	0.434	-	-	-
K_g	-	1.26×10^{-7}	-	-	-

Figure 5.27 compares the recharge-conductivity ratio and the conductivity-porosity ratio for the generated distributions to the base-case values. Recall that in the base case, $K = 1.38 \times 10^{-2}$ m/day, $Rech = 5.48$ cm/year, and $\theta = 5.0 \times 10^{-4}$. The plots in Figure 5.27 illustrate how the two ratios ($Rech/K$ and K/θ) vary among the 260 realizations around the base-case ratios. As can be seen in the figure, $Rech/K$ varies from a minimum that is about 0.4 times the base-case ratio to a maximum that is about three times larger. The conductivity-porosity ratio varies from about 0.0 times the base-case value to about 50 times larger than the base-case value. More realizations lie above the base-case lines, which is a conservative selection, as the high K/θ ratios lead to earlier arrival of mass and less mass diffusion and decay.

FEFLOW is used to solve the density-driven flow problem for 260 realizations with the recharge, conductivity, and porosity values already generated. Macrodispersivity values are fixed at 100 m and 10 m in the longitudinal and transverse directions, respectively. Domain geometry and boundary conditions remain unchanged and are similar to the one used in Section 4. To assess the choice of the combined random values used in this analysis, the results of these realizations at locations of UAe-1, UA-1, and HTH-1 are analyzed. Figure 5.28 is a plot of the concentration and head profiles in UAe-1 in terms of the mean of the 260 realizations, the mean \pm one standard deviation, the base-case result and the measured data. The first observation in this figure is that the mean of the MC realizations predicts a higher transition zone than the base case (recall that the base case is different than the calibration case in the sense that chimney changes in porosity and conductivity are not incorporated in the calibration). The one standard deviation confidence interval encompasses all but one of the data points for the head at UAe-1, but is still above the clustered chloride concentration data at depths in excess of 1,600 m. The head data at UA-1 and HTH-1 are plotted against the simulation results in Figure 5.29. Again, the confidence interval in the figure

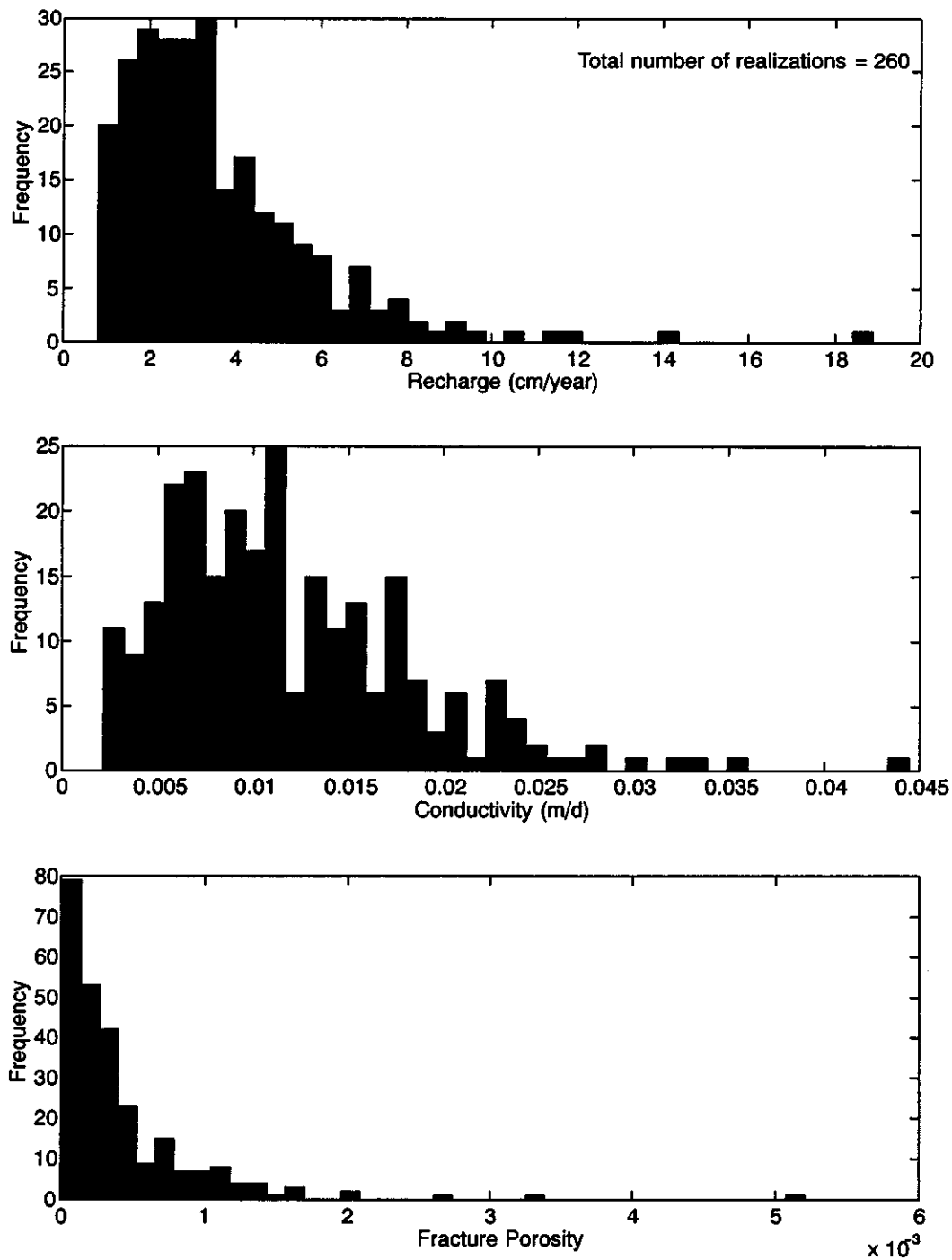


Figure 5.26. Randomly generated distributions for *Rech*, *K* and θ for the final Cannikin modeling stage.

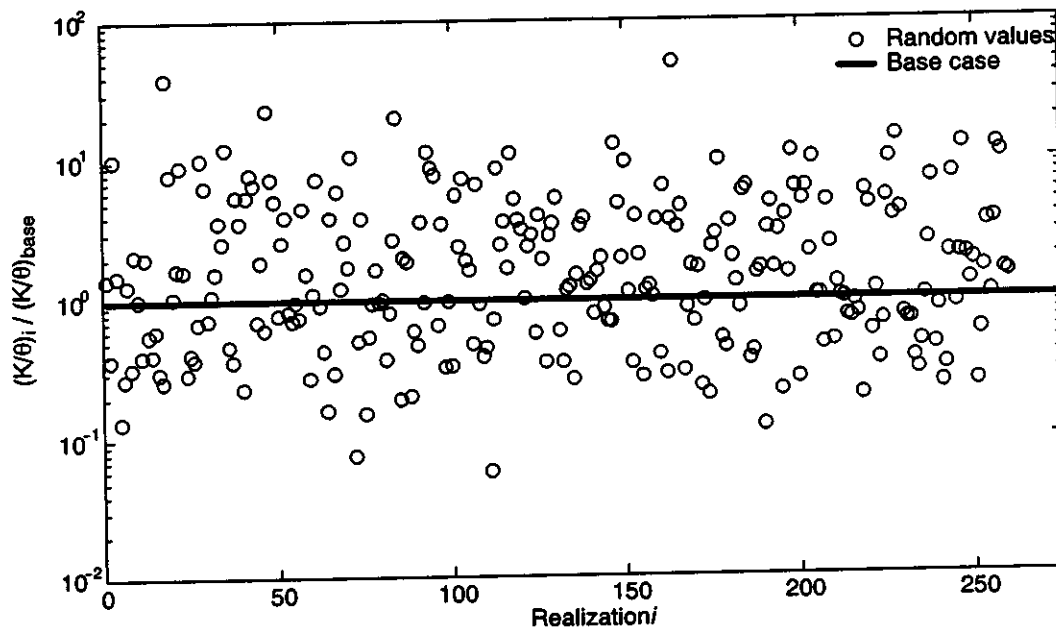
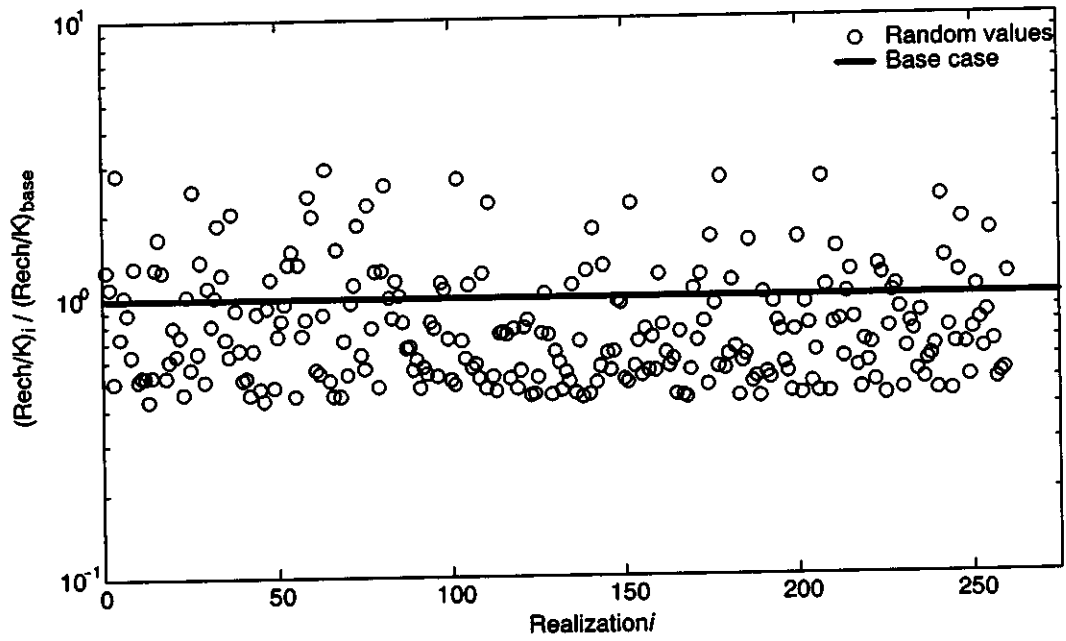


Figure 5.27. Comparison of the randomly generated recharge-conductivity and conductivity-porosity ratios relative to the Cannikin base-case values.

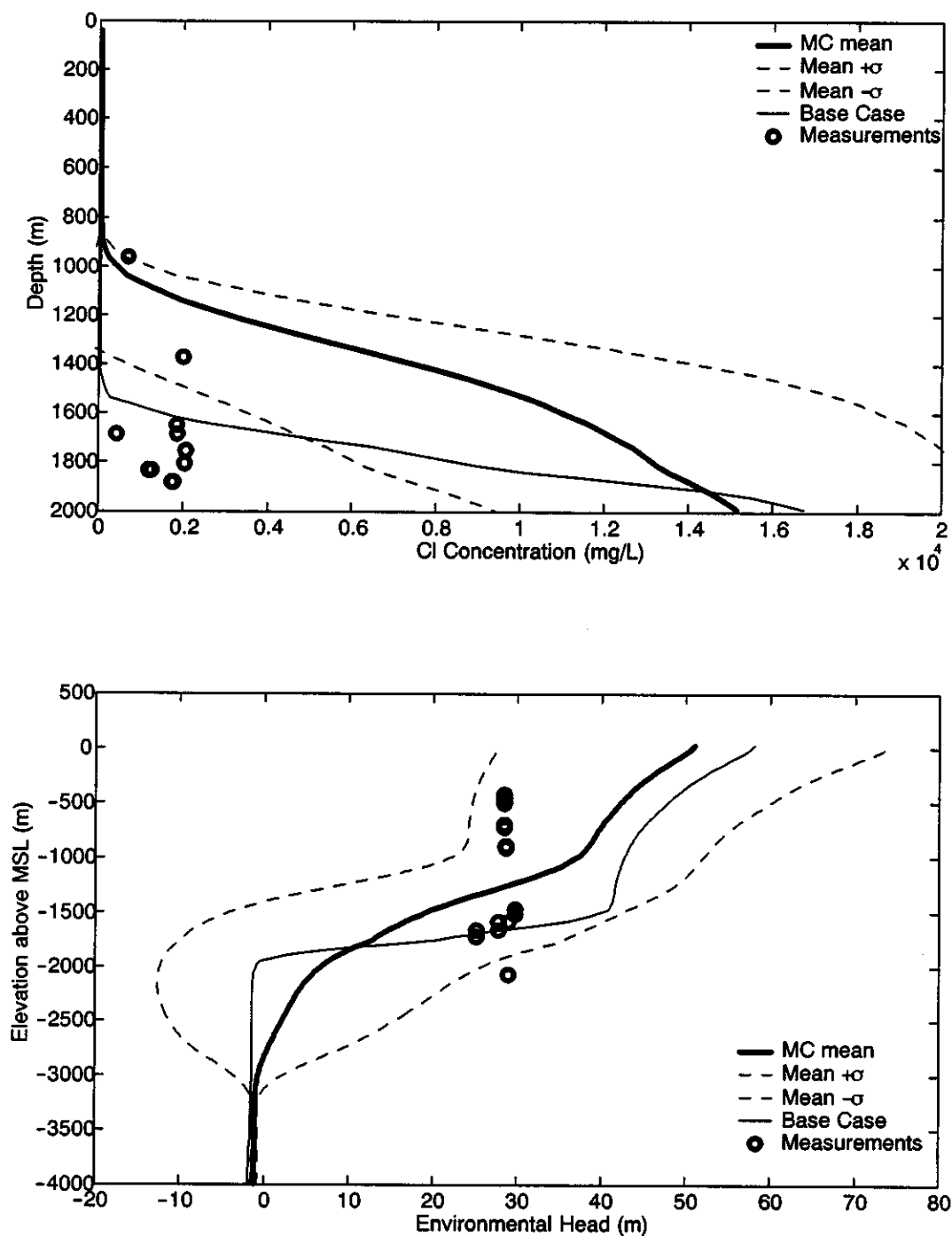


Figure 5.28. Sensitivity of UAc-1 modeled concentrations and heads to the combined uncertainties of $Rech$, K and θ in the final Cannikin modeling stage.

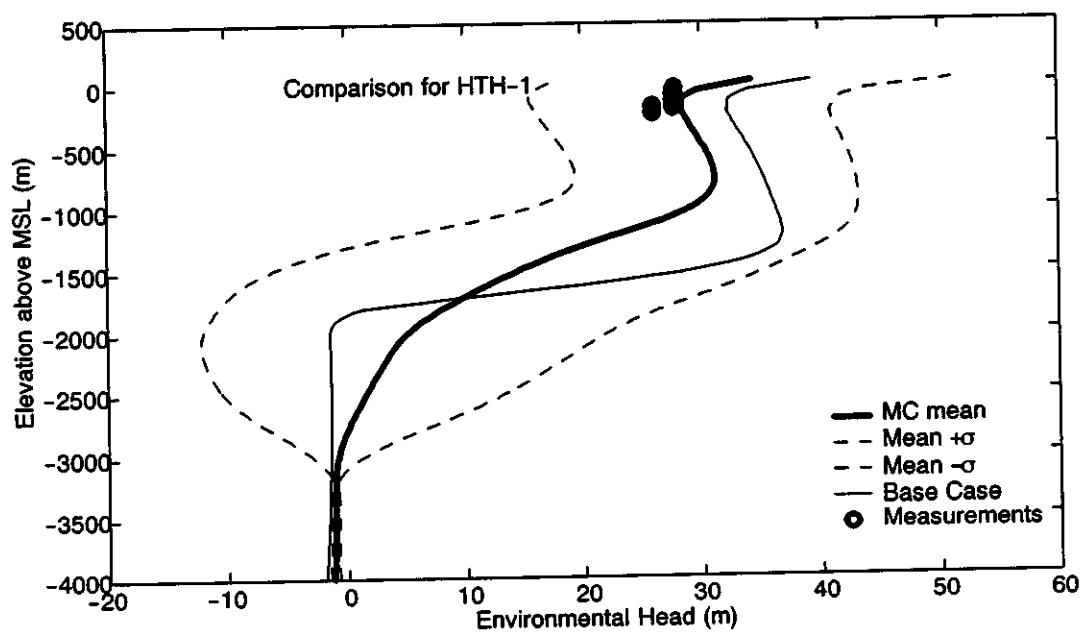
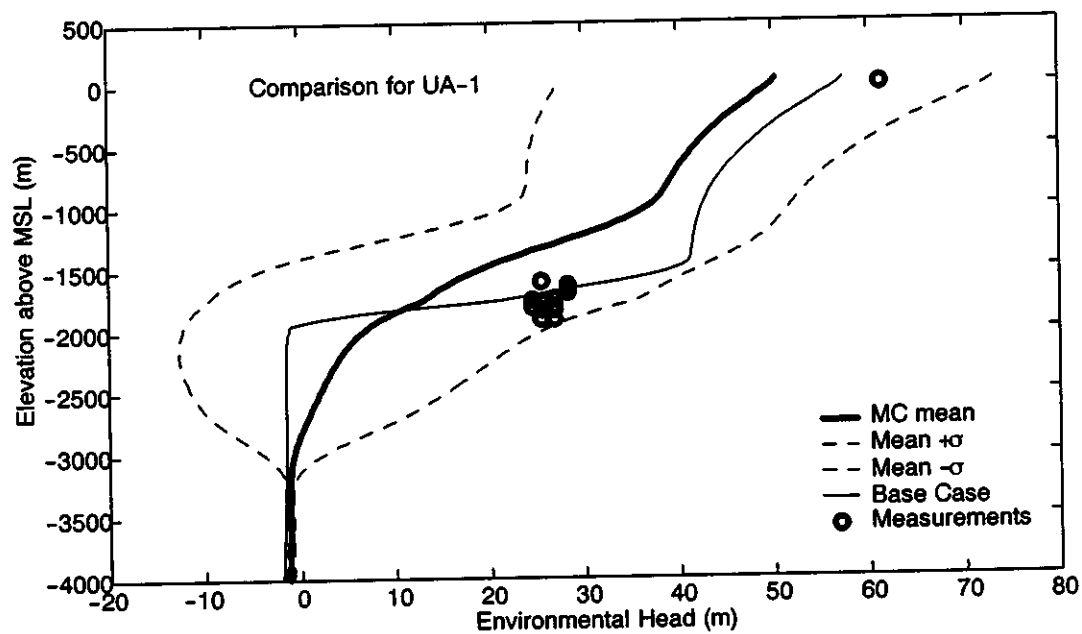


Figure 5.29. Sensitivity of UA-1 and HTH-1 modeled heads to the combined uncertainties of $Rech$, K and θ in the final Cannikin modeling stage.

encompasses all the head data at the two wells. The mean of the Monte Carlo simulations predicts a lower head at UA-1 and is a poorer match to the data than the base case, but it matches the HTH-1 head better than the base case. These comparisons indicate that the selected distributions of recharge, conductivity and porosity lead to a set of results with mean head distribution close to the wells' data and range of variability bounding all but one available data point. Again, since the quality of the concentration data is considered more questionable than that of the head data, and the concentration profile is more likely to violate the steady-state assumption, not matching the chemical data is tolerated for the modeling scenario for Cannikin.

Radionuclide transport simulations are also performed in a manner similar to Milrow and Long Shot. All transport parameters are kept constant in all realizations. Glass dissolution rate, k_g , is taken as $1.26 \times 10^{-7} \text{ day}^{-1}$, local dispersivities are fixed at 5.0 and 0.5 m, and the matrix diffusion parameter is assigned a value of 0.434 as discussed earlier. The particle-tracking simulations are performed for the same six cases and the same parameter values shown in Table 5.2. As was done for Milrow, the non-decayed transport results are discussed and the final decayed results are shown for a selected number of radionuclides.

5.3.1 Undecayed Transport Results

The undecayed breakthrough curves for the six solute classes with and without matrix diffusion are more or less similar to those presented for Milrow in Section 5.1. Therefore, there is no need to repeat the plot and the corresponding discussion here. The results that are of interest and importance to risk assessment studies are those related to the first arrival time and the location of the breakthrough. Similar to the analysis of Milrow, the 260 realizations are analyzed in terms of the percentage of mass that breaks through within 2,200 years, the first arrival time, the last arrival time, the duration of breakthrough, the location of the plume edges with respect to the bathymetric profile, the plume width, the location of the plume center after matrix diffusion computation, and the depths below MSL where breakthrough occurs. Figure 5.30 shows the distribution of the mass percentage that reaches the seafloor within the 2,200-year time frame. About 139 realizations out of 260 show less than 1 percent of the total mass reaching the breakthrough boundary. Out of these realizations, about 85 do not show any mass breakthrough. A total number of 157 realizations have less than 5 percent of the total mass out within that time frame, 175 have less than 10 percent of the mass out and only about 5 realizations have above 90 percent of the mass out.

Figure 5.31 displays the distributions of the first arrival time (whether it is for one particle or a thousand particles), the last arrival time and the duration of breakthrough. The figure shows that about 32 realizations (out of 260) show a first mass arrival within 60 years. Many realizations show a first arrival time less than 1,000 years. Again, about 85 realizations do not show any mass arrival within the simulation time. The figure also shows that about 140 realizations require a last arrival time beyond 2,200 years. For the breakthrough duration, most of the realizations that show a breakthrough have duration between 1,000 and 2,200 years. Figure 5.32 displays the distributions of the locations of the plume edges on the bathymetric profile, the plume width, and the distance from the groundwater divide to the center of the plume that is obtained after accounting for matrix diffusion effect. The location of the left (first) edge of the plume in many realizations is concentrated

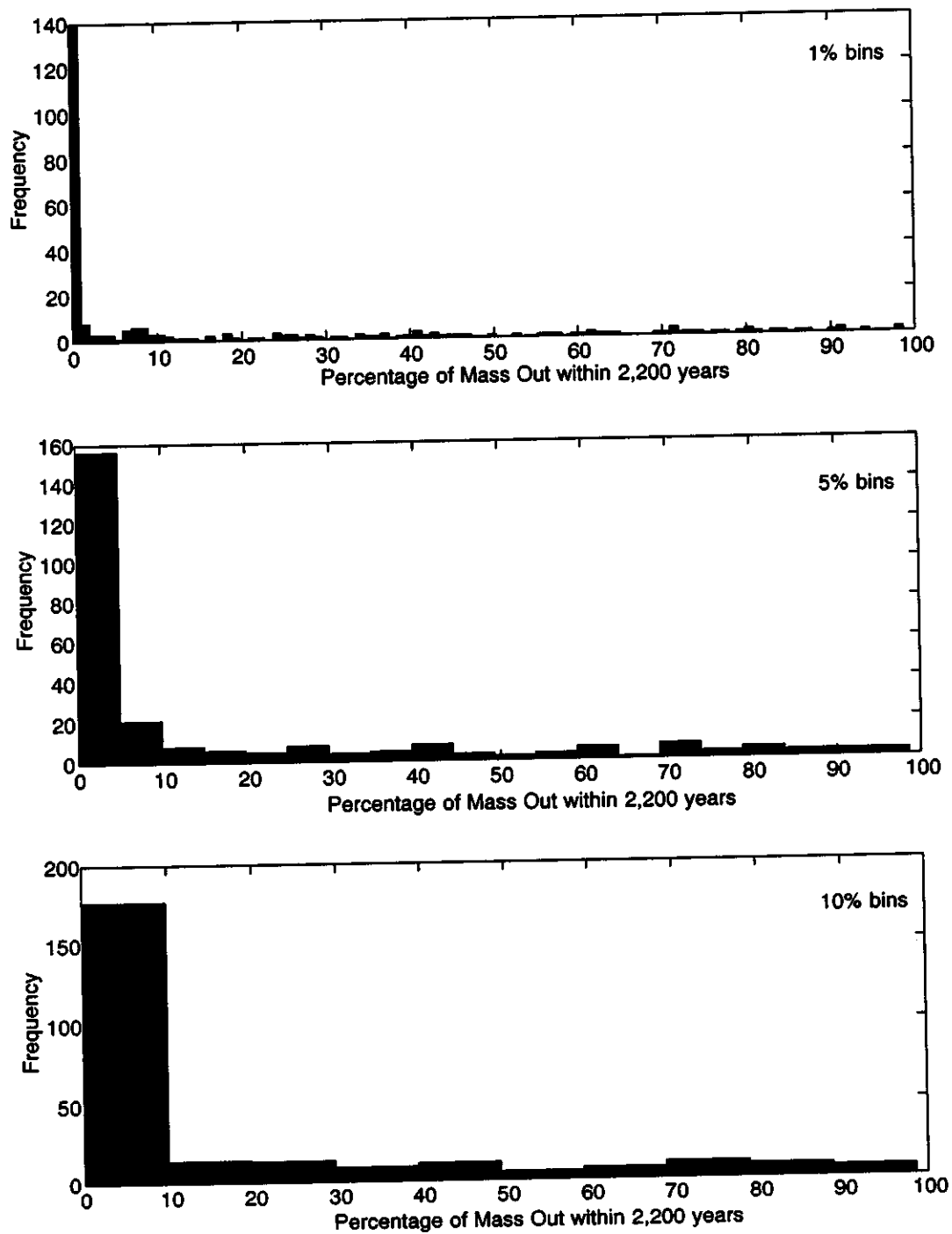


Figure 5.30. Histograms of the percentage of Cannikin mass that has broken through within 2,200 years.

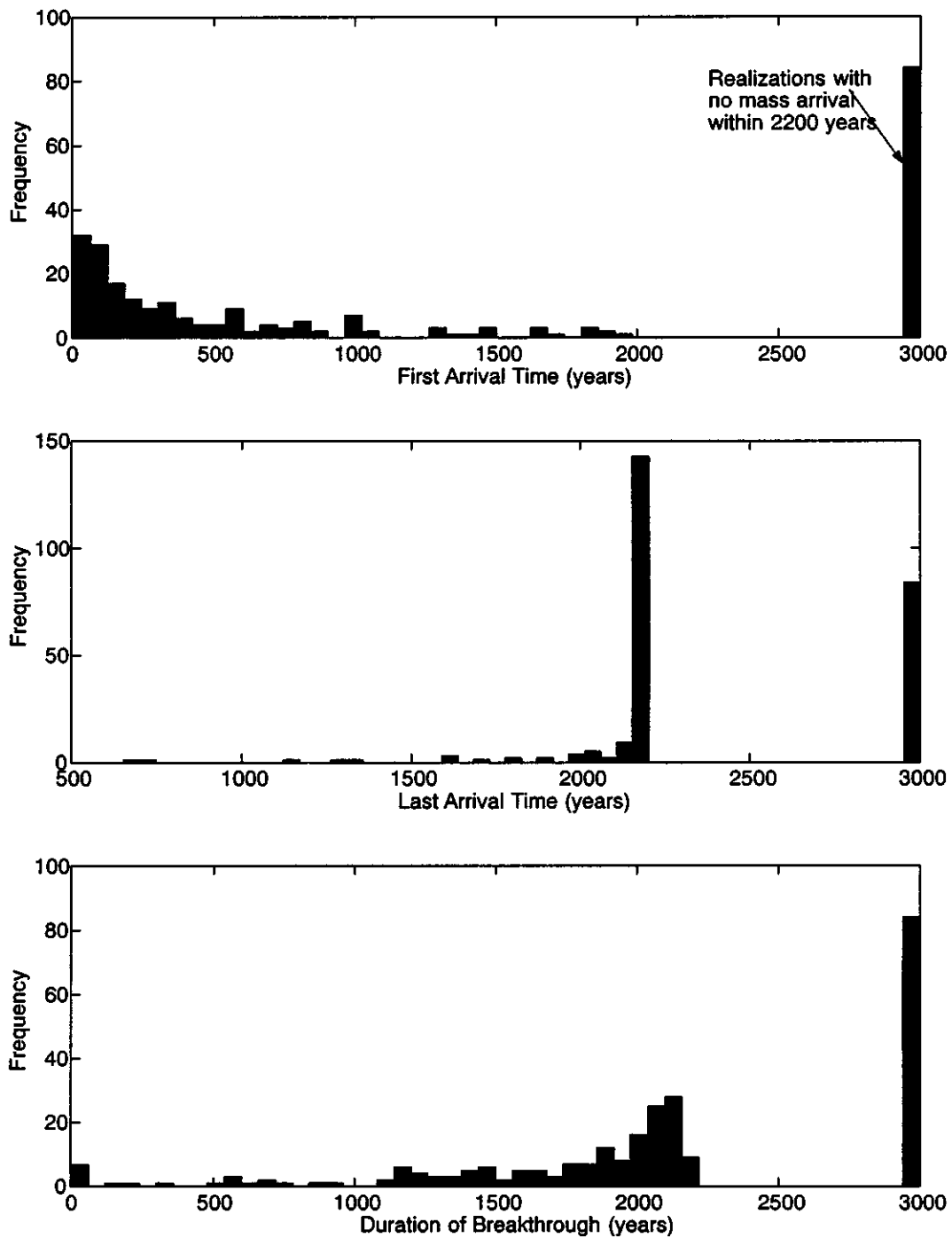


Figure 5.31. Histograms showing the distribution of first arrival time, last arrival time, and duration of breakthrough for Cannikin.

between 4,000 m and 5,000 m from the island centerline, while the right (second) edge of the plume is located within the range 4,600 m to 6,000 m. The location of the right edge of the plume shows more spread than the left edge. The breakthrough at Cannikin is spread over a length that varies from 200 m to about 1,800 m with no tendency toward certain width, whereas at Milrow many realizations showed a plume width between 400 and 800 m and at Long Shot the distribution of the plume width has peaks between 1,000 and 1,200 m.

The last quantity in Figure 5.32 is the distance from the divide to the plume center. When accounting for matrix diffusion, about 225 realizations (out of 260) did not contribute to the final breakthrough results at Cannikin. This number is to be compared to 240 (out of 300) at Milrow and 117 (out of 240) at Long Shot. These realizations have late arrival and slow groundwater velocities, which increase the residence time of the mass in the fractured system and allow for more diffusion into the matrix as opposed to the realizations with early arrival and high velocities. These latter realizations are only 35 in Cannikin and as such one would expect the Cannikin breakthrough results to have the lowest mass flux and concentration values.

Figure 5.33 shows the distribution of the depth below MSL of the plume edges where breakthrough occurs. This information is very important for risk assessment studies as it helps determine the nature of the currents that disperse the flowing mass and the type of sea creatures living at these depths. The figure shows that the left edge of the plume exists at a depth of 45 to 75 m, whereas the right edge exists at a depth of 50 to 80 m below MSL. Breakthrough at Milrow occurs at depths ranging from 2 to about 25 m and at Long Shot it occurs at depths between 20 to 70 m. The different depths at the three tests are a result of the different bathymetric profiles as can be seen from Figure 2.9.

5.3.2 Transport Results with Radioactive Decay

For all 12 radionuclides representing the first five cases, the transport results are tabulated in Tables 5.8a and 5.8b. The tables are similar to Tables 5.3a and 5.3b presented earlier for Milrow. Figure 5.34 depicts the flux and concentration results for tritium, ^3H , which is an element in Case 1, with a matrix diffusion parameter value of 0.434. The mean concentration distribution has a peak value of about 1.9×10^{-9} times the initial source concentration, C_0 . Adding one standard deviation to this value leads to a normalized peak of about 3.0×10^{-8} . This peak occurs roughly at 100 years after the test and about 5,300 m from the island center (about 2,970 m from the shoreline). These normalized concentrations are about one order of magnitude lower than those for Milrow. A ten-year later arrival time and a more spreading of mass cause this concentration reduction in comparison with Milrow. In comparison to Long Shot, Cannikin fluxes and concentrations for ^3H are about five to six orders of magnitude lower. The results for ^{14}C , shown in Figure 5.35, show significant mass flux and peak concentration as compared to ^3H with $\kappa = 0.434$. The normalized peak of the mean concentration is found to be about 9.0×10^{-5} , and occurs at about 1,200 to 1,500 years and at 5,500 m from the groundwater divide. These values are less than an order of magnitude lower than at Milrow and about two orders of magnitude lower than at Long Shot.

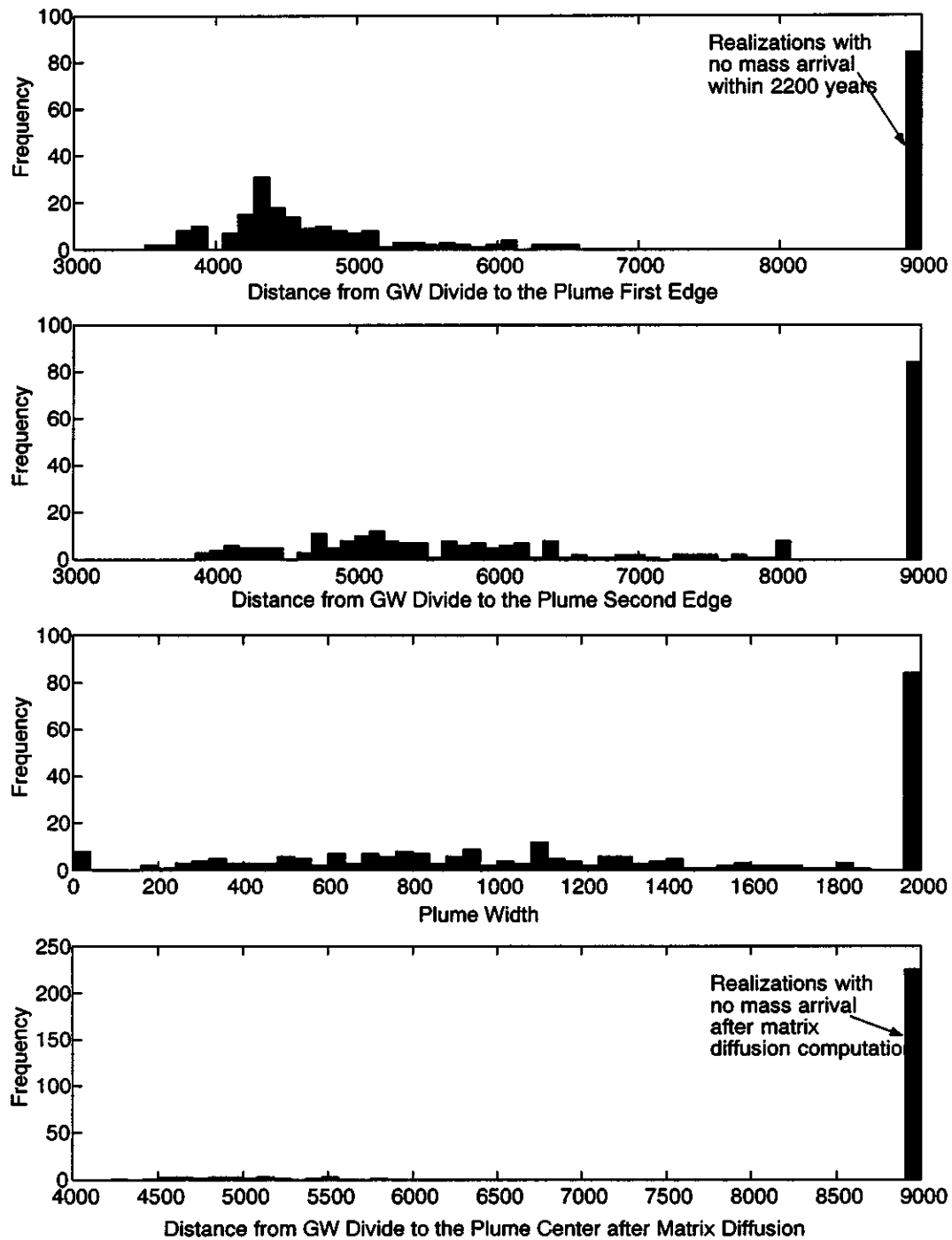


Figure 5.32. Histograms showing the distance from groundwater divide to plume edges and plume width for Cannikin.

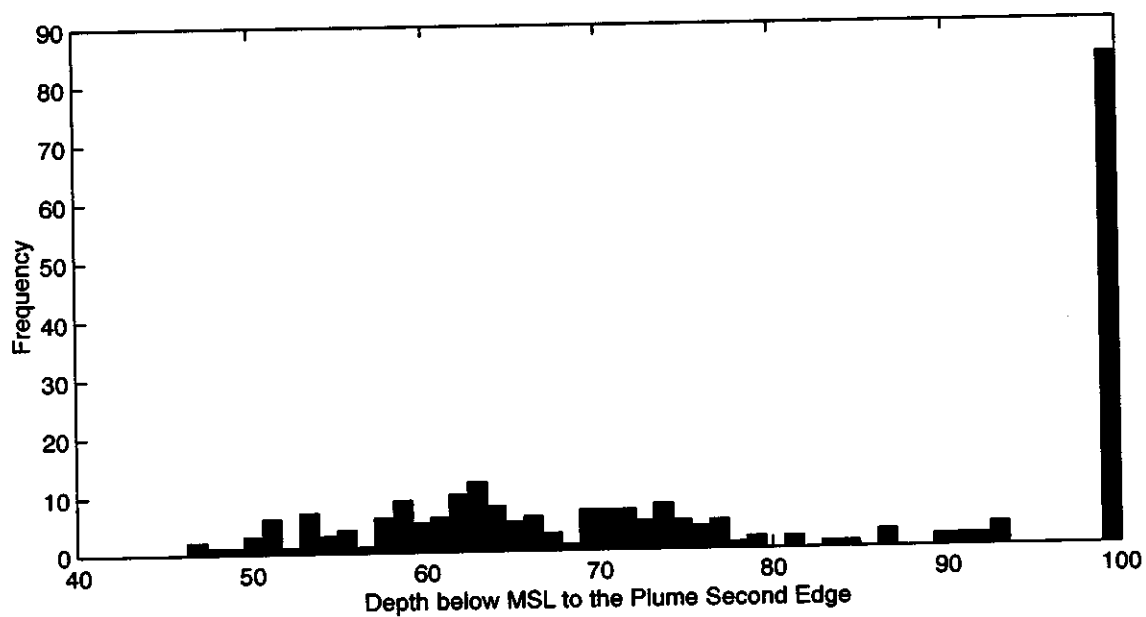
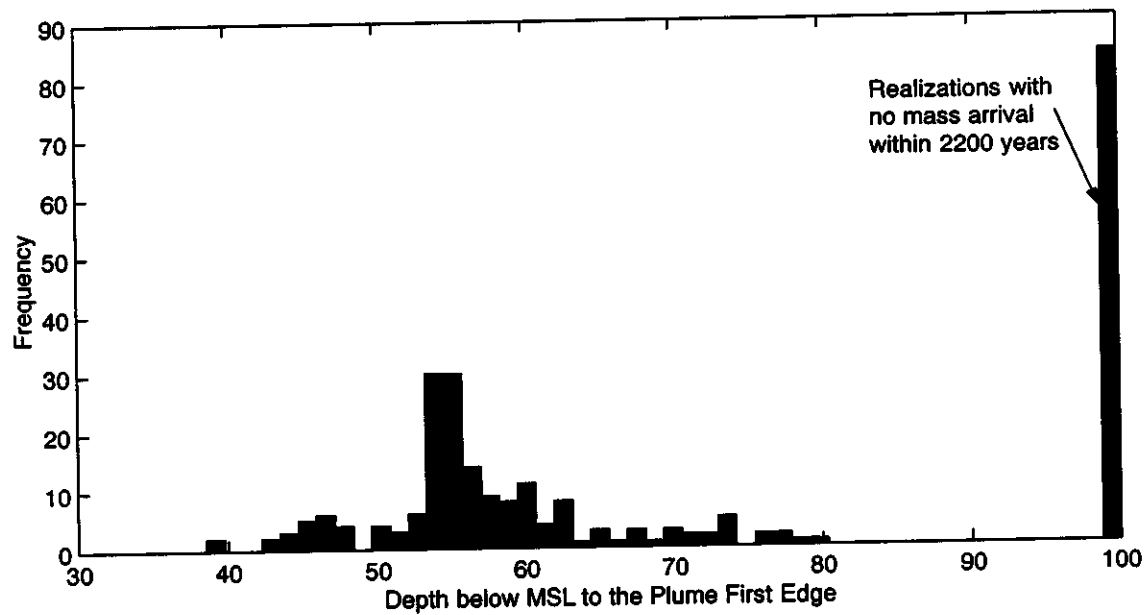


Figure 5.33. Histograms showing the distributions of depths below MSL at which the plume edges discharge to the ocean floor for Cannikin.

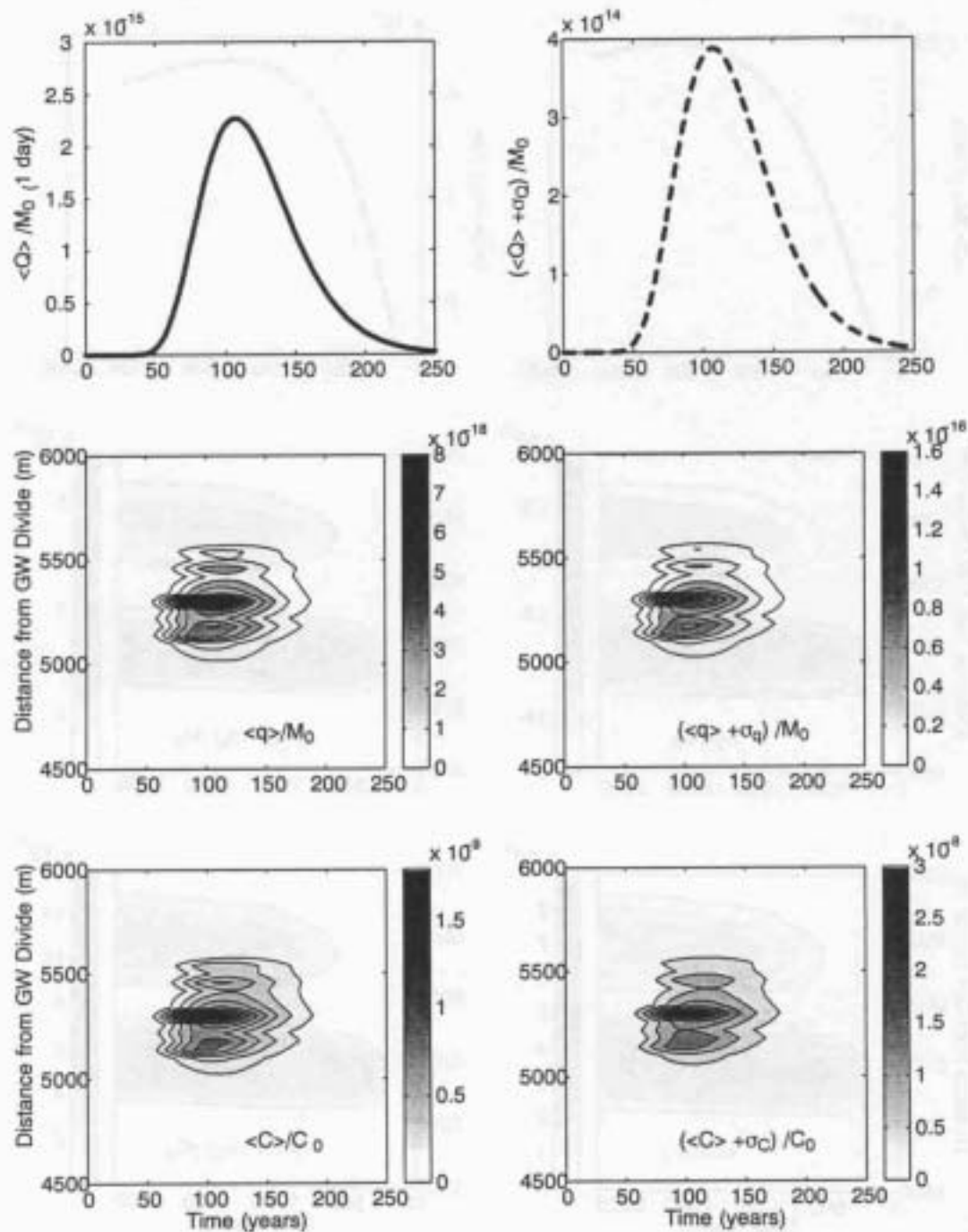


Figure 5.34. Statistics of mass flux and concentration for ^3H from Cannikin with $\kappa = 0.434$.

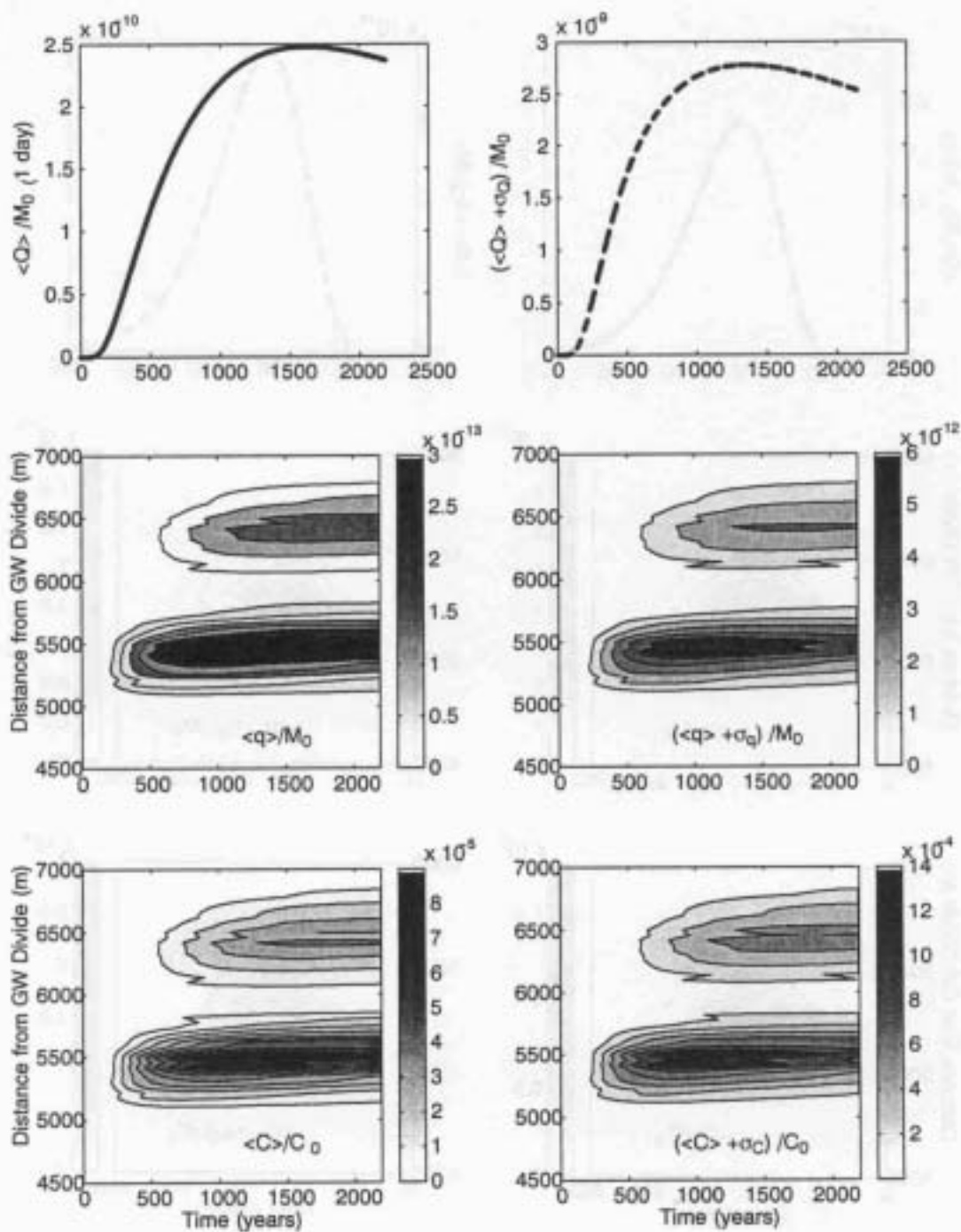


Figure 5.35. Statistics of mass flux and concentration for ^{14}C from Cannikin with $\kappa = 0.434$.

Table 5.8a. Peaks of expected and standard deviation of mass flux and the associated times and locations for radionuclides in the Cannikin source term. The elements in Class 6 are completely decayed.

Case	Radio-nuclide	Half-life	$\langle Q \rangle_{\max}$	Time	$(\sigma_Q)_{\max}$	Time	$\langle q \rangle_{\max}$	Time	Location	$(\sigma_q)_{\max}$	Time	Location
1	^3H	4.49e+03	2.2682e-015	1.0740e+002	3.6498e-014	1.0740e+002	9.5484e-018	1.0137e+002	5.3000e+003	1.5367e-016	1.0137e+002	5.3000e+003
	^{14}C	2.09e+06	2.4789e-010	1.6241e+003	2.5332e-009	1.3315e+003	3.9393e-013	1.1140e+003	5.4200e+003	5.8704e-012	9.9781e+002	5.4200e+003
	^{85}Kr	3.91e+03	9.5301e-016	1.0027e+002	1.5336e-014	1.0027e+002	4.2107e-018	9.4795e+001	5.3000e+003	6.7765e-017	9.4795e+001	5.3000e+003
	^{85}Rb	stable	3.0916e-010	2.0910e+003	3.0316e-009	1.6762e+003	4.5874e-013	1.5753e+003	5.5000e+003	6.6673e-012	1.1140e+003	5.4200e+003
2	^{36}Cl	1.10e+08	1.5005e-010	2.1008e+003	1.4728e-009	1.6921e+003	2.2169e-013	1.2975e+003	5.4200e+003	3.2278e-012	1.1293e+003	5.4200e+003
	^{129}I	5.73e+09	1.5077e-010	2.1145e+003	1.4784e-009	1.7014e+003	2.2234e-013	1.3025e+003	5.4200e+003	3.2361e-012	1.1332e+003	5.4200e+003
3	^{90}Sr	1.06e+04	9.2055e-014	1.6712e+002	1.4767e-012	1.6658e+002	2.8592e-016	1.5342e+002	5.2200e+003	4.6013e-015	1.5342e+002	5.2200e+003
	^{90}Y	2.67e+00	2.3193e-017	1.6712e+002	3.7206e-016	1.6658e+002	7.2037e-020	1.5342e+002	5.2200e+003	1.1593e-018	1.5342e+002	5.2200e+003
	^{90}Zr	stable	1.8335e-010	2.1036e+003	1.7993e-009	1.6926e+003	2.6601e-013	1.6488e+003	5.5000e+003	3.8095e-012	1.0230e+003	5.3800e+003
4	^{99}Tc	7.78e+07	6.2483e-011	2.0751e+003	6.1458e-010	1.6559e+003	1.0465e-013	1.3441e+003	5.4600e+003	1.5554e-012	9.8082e+002	5.3800e+003
5	^{137}Cs	1.10e+04	1.4743e-013	1.7041e+002	2.3636e-012	1.6986e+002	4.6180e-016	1.6767e+002	5.3800e+003	7.4319e-015	1.6767e+002	5.3800e+003
	^{137}Ba	stable	2.4861e-010	2.0816e+003	2.4408e-009	1.6641e+003	3.6183e-013	1.7556e+003	5.5400e+003	5.0924e-012	1.2038e+003	5.4600e+003

Table 5.8b. Peaks of expected and standard deviation of concentration and the associated times and locations for radionuclides in the Cannikin source term. The elements in Class 6 are completely decayed.

Case	Radio-nuclide	Half-life	$\langle C \rangle_{\max}$	Time	Location	$(\sigma_C)_{\max}$	Time	Location	σ_{Time}	σ_{Location}
1	^3H	4.49e+03	1.9520e-009	1.0137e+002	5.3000e+003	3.1415e-008	1.0137e+002	5.3000e+003	2.0833e+002	6.5065e+002
	^{14}C	2.09e+06	9.4683e-005	1.2838e+003	5.5000e+003	1.3577e-003	1.0975e+003	5.5000e+003	2.0833e+002	6.5065e+002
	^{85}Kr	3.91e+03	8.6081e-010	9.4795e+001	5.3000e+003	1.3853e-008	9.4795e+001	5.3000e+003	2.0833e+002	6.5065e+002
	^{85}Rb	stable	1.1226e-004	1.5589e+003	5.5000e+003	1.5655e-003	1.2712e+003	5.5000e+003	2.0833e+002	6.5065e+002
2	^{36}Cl	1.10e+08	5.1929e-005	1.5792e+003	5.5400e+003	7.1875e-004	1.1293e+003	5.4200e+003	2.1508e+002	6.3753e+002
	^{129}I	5.73e+09	5.2114e-005	1.5858e+003	5.5400e+003	7.2059e-004	1.1315e+003	5.4200e+003	2.1508e+002	6.3753e+002
3	^{90}Sr	1.06e+04	5.4407e-008	1.5342e+002	5.2200e+003	8.7559e-007	1.5342e+002	5.2200e+003	2.1375e+002	6.2121e+002
	^{90}Y	2.67e+00	1.3708e-011	1.5342e+002	5.2200e+003	2.2060e-010	1.5342e+002	5.2200e+003	2.1375e+002	6.2121e+002
	^{90}Zr	stable	6.5042e-005	1.6345e+003	5.5000e+003	8.8996e-004	1.3874e+003	5.5000e+003	2.1375e+002	6.2121e+002
4	^{99}Tc	7.78e+07	2.3241e-005	1.3392e+003	5.4600e+003	3.1998e-004	1.1293e+003	5.4600e+003	2.1472e+002	6.1975e+002
5	^{137}Cs	1.10e+04	9.4409e-008	1.6767e+002	5.3800e+003	1.5193e-006	1.6767e+002	5.3800e+003	2.0988e+002	6.2908e+002
	^{137}Ba	stable	8.8172e-005	1.7288e+003	5.5400e+003	1.1855e-003	1.2849e+003	5.5000e+003	2.0988e+002	6.2908e+002

5.3.3 Summary and Discussion

The numerical modeling for the test at Cannikin is performed in two stages: a calibration stage and a final modeling stage. The calibration utilized chloride concentration data from one well and head data from three wells. As the quality of the concentration data was questionable, a focus was placed on getting a close match to the head data regardless of how the simulated concentrations compare to the measurements. Calibration indicated that the heads at Cannikin are higher than at Milrow and Long Shot, and the transition zone should therefore be deeper. This resulted in recharge and conductivity values higher than those used for the base case at Milrow. The final modeling resulted in a mean head distribution closer to the data than the base case and the calibration case at the same locations, but more deviating at other locations. The confidence interval around that mean encompasses all the head data for the three wells.

Transport results indicated that the radionuclides' movement at Cannikin is only slightly slower than Milrow (on average). That may be attributed to the location and size of the cavity. The Milrow cavity extends for 212 m in the two directions, whereas the Cannikin cavity is about 355 m on a side. Also, the working point at Milrow is located at about 1,218 m and that of Cannikin is at about 1,791 m below ground surface. This leads to longer travel distances in the case of Cannikin, which leads to a later arrival of mass to the breakthrough boundary as compared to Milrow. The flux and concentration values at Cannikin change from less than an order of magnitude to about an order of magnitude lower than Milrow, and from two to about five orders of magnitude lower than Long Shot results.